Separation and Purification Technology 376 (2025) 133894

Contents lists available at ScienceDirect

Separation and Purification Technology

journal homepage: www.elsevier.com/locate/seppur

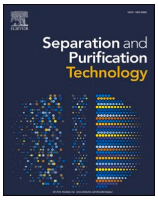

Enhanced performance of hierarchical porous HKUST-1/g-C_3N_4 heterostructure in the degradation of antibiotics with and without light

Liqin Nie [a,b,c,1], Kaige Wang [a,b,c,1,*], Wei Zhao [a,b,c], Chen Zhang [a,b,c], Tiehan Shen [d,*]

[a] Key Laboratory of Photoelectronic Technology of Shaanxi Province, Xi'an, China
[b] National Center for International Joint Research of Photoelectric Technology & Nano-Functional Materials and Application, Xi'an, China
[c] Institute of Photonics and Photon-Technology, Northwest University, Xi'an, China
[d] Joule Physics Laboratory, School of Science, Engineering and Environment, University of Salford, Salford, Greater Manchester M5 4WT, UK

ARTICLE INFO

Keywords:
HKUST-1
Graphitic carbon nitride
Molecular oxygen activation
Tetracycline hydrochloride removal
Light-free environment

ABSTRACT

Currently, the advanced oxidation processes (AOPs) for water treatment are limited by the demand on externally supplied oxidants or illumination. To overcome these constraints, a series of micro-nano-composites composed of a copper-based metal–organic framework 'HKUST-1' and graphitic carbon nitride (g-C_3N_4) nanosheets, were designed and synthesized via electrostatic self-assembly, hydrothermal treatment and decarboxylation. These hierarchical porous catalysts (HP-HKUST-1/g-C_3N_4) exhibit outstanding characteristics, particularly, in the degradation of Tetracycline Hydrochloride (TCH) under either total darkness or visible illumination. Experimental results demonstrate that TCH can be effectively degraded without externally supplied oxidant. Under dark conditions, 30 mg of the catalyst removed 99.92% of 50 mL 50 mg·L^{-1} TCH in 30 min; under visible light, 99.95% degradation was achieved in just 20 min. The exceptional performance is attributed to high Cu(I) content which offer strong reducing power to activate O_2 to generate H_2O_2. Additionally, photoexcited electrons in g-C_3N_4 transfer to HKUST-1 via heterojunctions, which suppresses the recombination of electron-hole pairs in g-C_3N_4 and supplies extra electrons for the O_2 reduction in HKUST-1. This study not only presents ideas for designing highly efficient catalysts with self-produced H_2O_2 by activating O_2, but also proposes a practical pathway towards the development of AOPs for wastewater treatment.

1. Introduction

Antibiotics, as a class of highly effective antimicrobial agents, are widely used in the prevention and treatment of various human or animal diseases [1,2], in the promotion of individual growth, increase of crop yields, medical care, livestock production and aquaculture [3,4]. On the other hand, antibiotics generally have stable chemical structures and are resistant to biodegradation [5]. They can be excreted from organisms in an active form, accumulating within surface and groundwater, and the residues can reach μg·L^{-1}, which will cause long-term harm to human health [6]. Much worse, antibiotics can also inhibit the growth and development of aquatic species and disrupt the balance of the ecosystem [7]. Therefore, the development of methodologies to eliminate thoroughly and efficiently antibiotic residues in water bodies in an environmentally friendly manner has attracted widespread attention around the world.

Currently, the conventional methods for removing antibiotics from water bodies mainly include biological treatment [8], chlorination treatment [9] and adsorption treatment [10]. All these methods have their disadvantages such as high cost, highly toxic by-products and low efficiency, which remains problematic in their applications [11]. In recent years, advanced oxidation processes (AOPs) [12], an advanced wastewater treatment technology that uses strong oxidants to convert organic substances into inorganic ones, have been developed and applied in the degrading of antibiotics [13]. Its main mechanism is to generate strong oxidants which then degrade antibiotics and convert them into small-molecular substances. The efficiency of this method in removing antibiotics is several times better than that of the traditional treatment methods [14].

In the process of rapid development, AOPs are facing some

---

* Corresponding authors.
E-mail addresses: wangkg@nwu.edu.cn (K. Wang), t.shen@salford.ac.uk (T. Shen).

[1] These authors contributed equally to this work.

https://doi.org/10.1016/j.seppur.2025.133894
Received 3 April 2025; Received in revised form 21 May 2025; Accepted 4 June 2025
Available online 6 June 2025
1383-5866/© 2025 The Authors. Published by Elsevier B.V. This is an open access article under the CC BY license (http://creativecommons.org/licenses/by/4.0/).

difficulties and problems that need to be solved urgently [15]. They require a large amount of energy to generate sufficient active oxidants, and major parameters such as appropriate temperature, pH value and oxidant concentration is necessary to control to ensure the effectiveness and stability of the reaction. Furthermore, in practical application, they require to add external oxidants such as hydrogen peroxide (H_2O_2), peroxysulfate (PS) or peroxymonosulfate (PMS), which may leave residual oxidants and lead to greater costs of removing pollutants [16,17].

One of the promising solution involves utilizing semiconductor photocatalysts to generate H_2O_2 through photogenerated electron-mediated O_2 activation [18–20]. When photocatalysts are photoexcited, the generated electrons (e^-) and holes (h^+) can react with water or oxygen molecules to form reactive oxygen species (ROS) such as hydroxyl radicals (·OH), superoxide radicals ($\cdot O_2^-$), and H_2O_2. And another valuable approach involves utilizing the strong reducibility of nano zero-valent iron, aluminum, and copper to activate molecular oxygen, which can be used to generate ROS under light-free conditions [21,22]. In addition, metal-derived materials have also been employed for molecular oxygen activation [23]. It has been reported that a typical copper-based metal–organic framework (MOF) material, known as HKUST-1, can generate a mixture of Cu^{2+}/Cu^+ metal ions in a solution environment [24], and the reducing capability of Cu(I) facilitates single-electron transfer to activate surface-adsorbed O_2, leading to generate H_2O_2 [25]. And more, graphitic carbon nitride (g-C_3N_4), a semiconductor material of emerging distinctive advantages [26–28], has been used to form a heterostructure with another semiconductor to enhance photogenerated electron transfer efficiency through the interfacial effect of heterojunction, thereby improving molecular oxygen (O_2) activation performance. [29].

To explore the structural characteristics of g-C_3N_4 and HKUST-1 and their roles in molecular oxygen activation, we have investigated the composite combination of HKUST-1 and g-C_3N_4 via a combination of hydrothermal synthesis and decarboxylation modification. A series of heterogeneous porous (HP)-HKUST-1/g-C_3N_4 with different mass ratios of HKUST-1 and g-C_3N_4, and their structural and chemical characterization, and their performance and mechanism in the efficient degradation of TCH under darkness and visible illumination are investigated in detailed. Furthermore, a comparative study was conducted between synthesized HP-HKUST-1/g-C_3N_4 in the present work and other MOF/g-C_3N_4-based photocatalysts to evaluate their catalytic efficiencies [30–35].

2. Experimental

2.1. Chemicals

Melamine ($C_3H_6N_6$), $Cu(NO_3)_2 \cdot 3H_2O$, absolute ethanol (C_2H_6O), potassium iodide (KI) and isopropyl alcohol (IPA) were purchased from Kermel Chemical Reagent Co., Ltd (Tianjin, China). 1,3,5-tricarboxylic acid (H_3BTC), p-Benzoquinone(p-BQ) were purchased from Macklin Chemical Reagent Co., Ltd (Shanghai, China). Tetracycline Hydrochloride (TCH) was purchased from Aladdin Reagent Co., Ltd. N,N-dimethylformamide (DMF) was purchased from Tianli Chemical Reagent Co., Ltd (Tianjin, China). Ethylenediamine tetraacetic acid disodium (EDTA-2Na) was purchased from Kaitong Chemical Reagent Co., Ltd (Tianjin, China). Potassium bromate ($KBrO_3$) was purchased from Aopusheng Chemical Co., Ltd (Tianjin, China). Potassium hydrogen phthalate ($C_8H_5O_4K$) was purchased from Baishi Chemical Co., ltd (Tianjin, China). All chemicals were analytical grade and used without further purification.

2.2. Preparation of catalysts

The synthesis of g-C_3N_4 nanosheets. The g-C_3N_4 nanosheet structure has a higher quantum efficiency and photocatalytic activity than that of the original bulk structure [36–40]. The crucible containing melamine was placed in a tube furnace (Boyuntong, TL1400, Nanjing, China) and heated at a rate of 5 °C/min in an air atmosphere to 550 °C, then maintained for 4 h, and a large amount of block-shaped g-C_3N_4 was prepared. Next, the prepared block-shaped g-C_3N_4 was ground and then heated to 550 °C under the same conditions for 2 h, g-C_3N_4 nanosheets were obtained.

The synthesis of HKUST-1. $Cu(NO_3)_2 \cdot 3H_2O$ was added to 50 mL mixed solution (water: ethanol: DMF = 1: 1: 1), and stirred for 15 min, which was labelled as Solution I. Subsequently, H_3BTC was added to the Solution I to form Solution II, maintaining a 2:1 mass ratio between $Cu(NO_3)_2 \cdot 3H_2O$ and H_3BTC. Then the Solution II was ultrasonically treated for 30 min, and after stirred ~6 h, it was transferred to a polytetrafluoroethylene reactor and heated at 90 °C in a sealed hydrothermal autoclave for 12 h, a kind of bluish precipitate was obtained. Subsequently, HKUST-1 would be obtained after the precipitate being filtered, washed with ethanol several times and dried at 90 °C in a vacuum drying oven for 12 h.

The synthesis of HP-HKUST-1/g-C_3N_4. Firstly, HKUST-1/g-C_3N_4 composites with different ratios were prepared by hydrothermal method using g-C_3N_4 nanosheets and HKUST-1, and these composites were labelled HK/CN-x, where "HK" stands for HKUST-1, "CN" stands for g-C_3N_4 and "x" represents the mass fraction of g-C_3N_4 nanosheets which were 25%, 50% and 75%, denoted as HK/CN-$_{25}$, HK/CN-$_{50}$, and HK/CN-$_{75}$, respectively. During this step, due to the negative charge of g-C_3N_4 nanosheets [41] in the solution and the positive charge on the surface of HKUST-1 [27,42], g-C_3N_4 nanosheets and HKUST-1 formed a HK/CN heterostructure through electrostatic self-assembly and hydrothermal synthesis, resulting in g-C_3N_4 nanosheets being coating on the HKUST-1. Then, the prepared HK/CN-x composites were subjected to a series of sequential treatments, i.e., decarboxylation, vacuum drying, and thermal treatment in a tube furnace under an air atmosphere. Finally, greenish powders, of HP-HKUST-1/g-C_3N_4 composites (labelled as HP-HK/CN-x where "HP" again stands for "hierarchical porous", namely, HP-HK/CN-$_{25}$, HP-HK/CN-$_{50}$ and HP-HK/CN-$_{75}$, respectively) were obtained. Fig. 1 illustrates diagrammatically the main processes for the preparation of the HP-HKUST-1/g-C_3N_4 heterojunction composites.

2.3. Characterization

The crystallographic structure of the sample was analyzed by X-Ray Diffraction (XRD) using a Bruker D8 ADVANCE X-ray diffractometer with Cu Kα radiation ($\lambda = 1.54056$ Å) with the 2θ range from 10° to 80°. Fourier transform infrared (FT-IR) spectra were collected on a Bruker INVENIO S spectrometer to determine the chemical structure. The morphologies of the sample were examined by a scanning electron microscopic (SEM, Thermo scientific, Apreo S), and a transmission electron microscopy (TEM, FEI, Tecnai G^2 F20). Energy Dispersive Spectrometer (EDS) was measured to detect the element composition of the sample. X-ray photoelectron spectroscopy of the as-prepared samples were analyzed on an X-ray photoelectron spectrometer (XPS, Thermo scientific, ESCALAB Xi^+). The specific surface area and pore size distributions were analyzed by a Micromeritics adsorption analyzer (Micromeritics, Multi-station ASAP2460, USA). The optical properties of the materials were investigated by means of the diffuse reflectance spectroscopy (DRS), using a SHIMADAZU (UV-3600Plus, Japan) spectrometer. The signals of active groups were detected by electron spin-resonance spectroscopy (ESR, Bruker, E500-9.5/12), where 5,5-Dimethyl-1-pyrroline-N-oxide (DMPO) aqueous solution was used as a paramagnetic species spin-trap agent. An Edinburgh FLS920 spectrophotometer equipped with a 450 W Xe lamp was employed to measure the Photoluminescence (PL) spectra of the samples. The photocurrent spectra were recorded on a CHI 660E electrochemical system (Shanghai, China) equipped with three standard electrodes: Pt as the counter electrode and Ag/AgCl as the reference electrode, the sample as the working electrode, and Na_2SO_4 (0.5 M) as the electrolyte. Sample powder was dispersed in 5 mL of deionized water by sonication. The

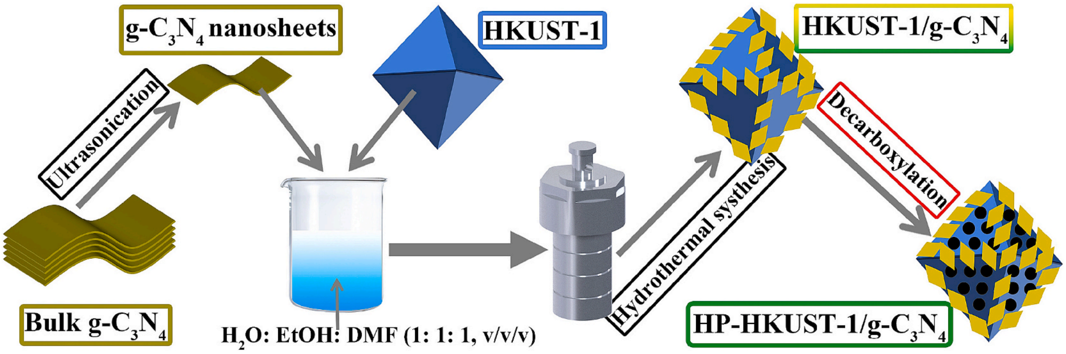

Fig. 1. Schematic illustration of the preparation of HP-HKUST-1/g-C_3N_4 heterostructure composite.

suspension was cover onto the surface of the fluorine-doped tin oxide (FTO) glass and dried under an infrared baking lamp to obtain the working electrode. A Xenon lamp (300 W) was used to simulate sunlight for photocurrent spectra measurement. Inductively coupled plasma-mass spectrometry (ICP-MS, Agilent, 7900ICP-MS) was employed to analyze the metal element content in the solution.

2.4. *Catalytic function*

The degradation of TCH by HP-HK/CN was investigated in dark and under illumination with a visible light source ($400 < \lambda < 780$ nm) (NBeT, HSX-F300, Beijing, China). Firstly, the catalysts (20/30/50 mg) were added respectively to TCH solution (50 mL, 50 mg·L^{-1}), and the catalytic activities of the materials were tested in a dedicated lighttight enclosure (see Fig. S4 in the Supplementary Materials for more details) under two conditions, i.e., maintained in total darkness for 30 min; exposed to visible illumination for 20 min at 25 °C. During this period, 2.5 mL of the solution was collected at 5 min time intervals, and the collected samples were centrifuged and the supernatant was taken. Then, the absorbance of TCH at the characteristic absorption wavelength of 357 nm was detected using an ultramicro spectrophotometer (Denovix, DS-11, USA). All tests were repeated three times to ensure accuracy. In addition, pure g-C_3N_4, HKUST-1 and HKUST-1/g-C_3N_4 were used instead of HP- HKUST-1/g-C_3N_4 as the controls. The absorbance is directly proportional to the concentration, and the degradation efficiency can be expressed as $(A_0 - A)/A_0 \times 100\%$, where A_0 represents the initial absorbance of the solution and A denotes the absorbance at different time intervals.

2.5. *Hydrogen peroxide production*

The amount of H_2O_2 produced by the catalyst was measured by iodometry [43]. Specifically, 30 mg of the catalyst was added to pure water, and at 5 min time interval, 3 mL of the suspension was taken, centrifuged, and the supernatant was collected. Potassium hydrogen phthalate ($C_8H_5KO_4$, 1 mL, 0.1 mol·L^{-1}) was added to the above solution

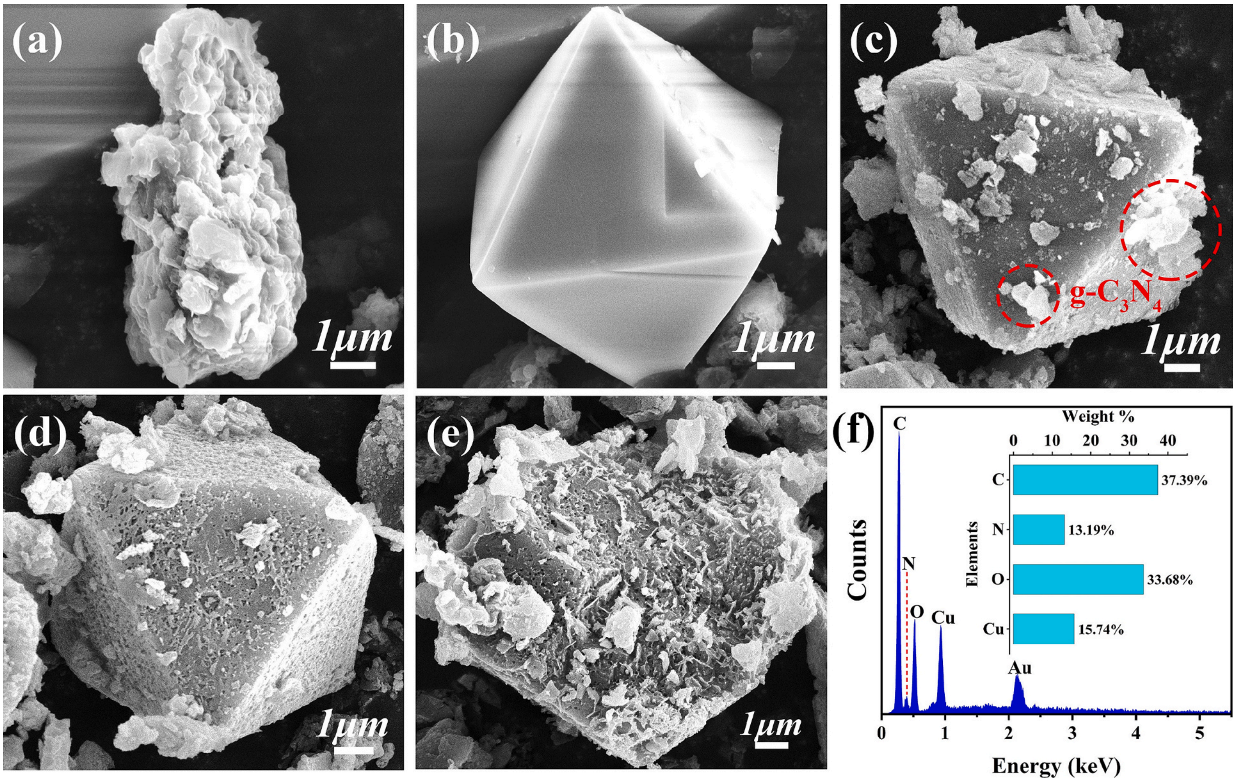

Fig. 2. Microstructure and morphology of the heterostructure composite. (a–e) SEM images of g-C_3N_4, HKUST-1, HKUST-1/g-C_3N_4, HP-HKUST-1/g-C_3N_4 and broken HP-HKUST-1/g-C_3N_4. (f) EDS of HP-HKUST-1/g-C_3N_4.

to maintain the acidic environment of the solution, forming solution 1. Then, KI (1 mL, 0.4 mol·L^{-1}) was added to solution 1 and kept for 30 min·H_2O_2 can react with I^- to form I_3^- ($H_2O_2 + 3I^- + 2H^+ \rightarrow I_3^- + 2H_2O$), and the absorbance of I_3^- can be measured at its characteristic peak (350 nm) by an ultraviolet–visible spectrophotometer (Denovix, DS-11, USA).

3. Results and discussion

3.1. Morphology and structure

In Fig. 2 typical sample microstructure images and composition analysis are shown. Fig. 2a shows the two-dimensional overlapping sheet structure of bulk g-C_3N_4, Fig. 2b, the octahedral shape of HKUST-1 crystals, and Fig. 2c, the HKUST-1/g-C_3N_4 formed by attaching g-C_3N_4 nanosheets on the surface of the HKUST-1. It can be observed from Fig. 2d and the high-resolution SEM image (Fig. S1, Supplementary materials) that, compared with HKUST-1 and HKUST-1/g-C_3N_4, many new mesopores and macropores have been formed on the surface of HP-HKUST-1/g-C_3N_4, indicating that the hierarchical porous structure has been successfully constructed. And the image of the broken HP-HKUST-1/g-C_3N_4 (Fig. 2e) is suggestive that the interior of the crystal has also become more porous. To further elucidate the microstructure of HP-HKUST-1/g-C_3N_4, high-resolution TEM (HRTEM) was employed to obtain detailed structural information, particularly regarding the interfacial contact between HKUST-1 and g-C_3N_4. As shown in Fig. S2 (Supplementary materials), g-C_3N_4 with a (002) lattice spacing of 0.32 nm was distributed on the HP-HKUST-1/g-C_3N_4 surface. HRTEM measurements show lattice fringes of ~0.25 nm in HP-HKUST-1/g-C_3N_4 corresponding to the (111) plane of Cu(I)/Cu(II), while the decarboxylated HKUST-1 appears amorphous. Fig. 2f is the Energy Dispersive Spectrometer (EDS) spectrum analysis of HP-HKUST-1/g-C_3N_4, showing that HP-HKUST-1/g-C_3N_4 contains four elements: C, N, O, and Cu (Au was added to enhance the conductivity of the sample) and indicating that g-C_3N_4 nanosheets and HKUST-1 have been successfully combined.

The porosity of the samples is further studied by nitrogen adsorption–desorption isotherms. It can be seen from Fig. 3a-c that the adsorption–desorption isotherms of all samples belong to the hybrid of type I and IV isotherms [44], indicating that g-C_3N_4 and HP-HKUST-1/g-C_3N_4 are of mesoporous materials. Furthermore, the isotherms of g-C_3N_4 (Fig. 3a) and HP-HKUST-1/g-C_3N_4 (Fig. 3c) display H3-type [35] adsorption hysteresis loops, indicating that g-C_3N_4, HKUST-1 and HP-HKUST-1/g-C_3N_4 have mesoporous and macroporous structures caused by their layered structure; while the isotherm of HKUST-1 has an H4-type [45] adsorption hysteresis loop, indicating that there are a large number of microporous in the HKUST-1. Fig. 3d shows the corresponding pore size distribution patterns.

The parameters on specific surface area, pore volume and pore diameter of the samples calculated by the Brunauer-Emmett-Teller (BET) and Barrett-Joyner-Halenda (BJH) methods [46] are listed in Table 1.

Table 1
Specific surface area, pore size and pore volume of the g-C_3N_4, HKUST-1 and HP-HKUST-1/g-C_3N_4.

Sample	Specific surface area (m^2/g) [a]	Pore/Micropore volume (cc/g) [b]	Average pore diameter (nm) [c]
g-C_3N_4	22.7569	0.148283/0.001084	17.0653
HKUST-1	1,200.3170	0.122610/0.514904	4.5195
HP-HKUST-1/g-C_3N_4	28.2505	0.122765/0.005182	19.9657

[a] The Brunauer-Emmett-Teller (BET) specific surface area;
[b] Pore volume measured under the condition of $P/P_0 = 0.99$;
[c] The Barrett-Joyner-Halenda (BJH) pore size from desorption branch of isotherm.

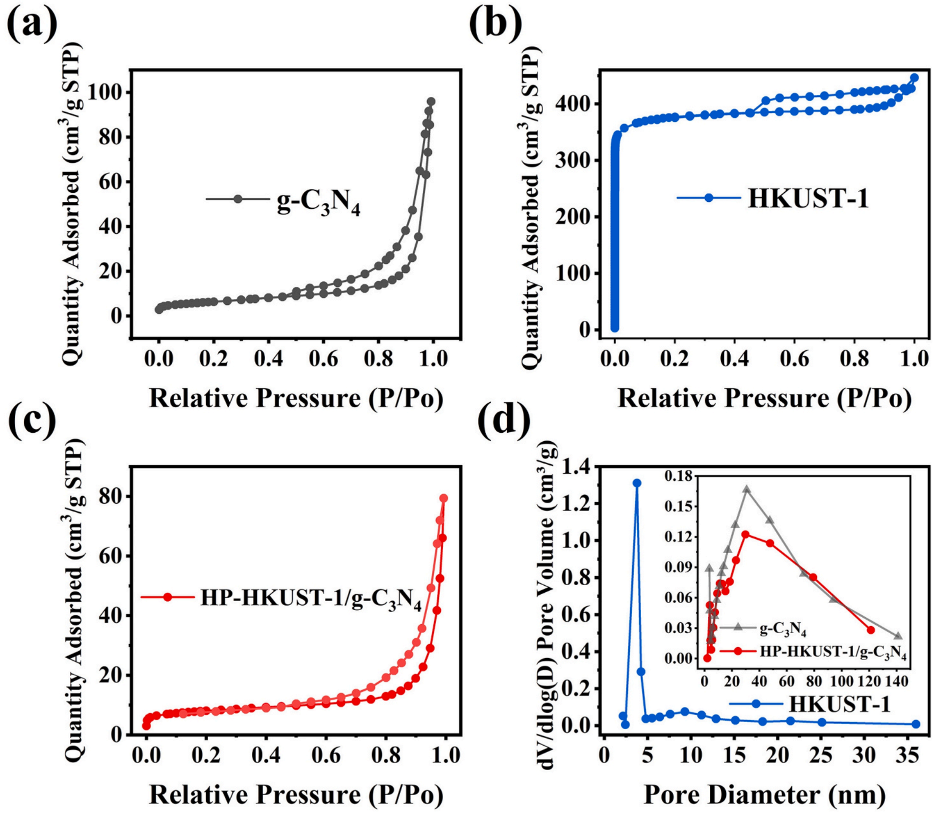

Fig. 3. Porous properties of the heterostructure composite. (a–c) N_2 adsorption–desorption isotherms of g-C_3N_4, HKUST-1 and HP-HKUST-1/g-C_3N_4. (d) Pore size distributions of HKUST-1, g-C_3N_4 and HP-HKUST-1/g-C_3N_4. The g-C_3N_4 content in the HP-HKUST-1/g-C_3N_4 composite was 50 wt%.

It can be seen from Table 1 that the specific surface area and micropore volume of HP-HKUST-1/g-C_3N_4 after decarboxylation are much smaller than that of HKUST-1, indicating that the micropores of the modified HKUST-1 have mostly been transformed into mesopores and macropores. In addition, the increase in the average pore diameter of HP-HKUST-1/g-C_3N_4 also indicates that a hierarchical porous structure has been established.

Fig. 4 shows the X-Ray Diffraction (XRD) pattern and Fourier Transform infrared spectroscopy (FT-IR) reflecting the crystal structure and chemical structure of HP-HKUST-1/g-C_3N_4.

As shown in Fig. 4a, the characteristic peaks of XRD of HKUST-1 and g-C_3N_4 at 11.83°, 17.32°, 19.24°, 26.15° and 27.69° can be observed in that of HP-HKUST-1/g-C_3N_4 samples with different percentage weight of HKUST-1 and are also presented in that of the HK/CN-$_{50}$ sample. The peak at 27.69° is attributed to the (002) crystal plane of g-C_3N_4, which is produced by the interlayer stacking. And the distinct peaks at 11.83°, 17.32°, 19.24° and 26.15° correspond to the four diffraction peaks of (222), (551), (440) and (731) crystal planes of HKUST-1 (CCDC 943008), respectively [47,48]. The relative intensity of the diffraction peaks of HP-HKUST-1/g-C_3N_4 varies with the mass ratio of the g-C_3N_4 and HKUST-1. The characteristic peaks of HKUST-1 in the HP-HKUST-1/g-C_3N_4 spectra did not shift, nor new peak was observed, indicating that the original crystal structure was unaltered during the preparation of the composites. Compared with both HKUST-1 and HK/CN-$_{50}$, the peak value of HP-HKUST-1/g-C_3N_4 at the (222) crystal plane decreased significantly, which is attributable to that the effect of the decarboxylation process. As the coordination bonds between the organic ligand H_3BTC and the metal clusters were broken, there is an increase in the mesoporous density and size generated in the (222) plane surface [49]. The expansion of pore and the distortion of some lattice units of the framework result in a reduction in the overall intensity of the diffraction peaks of the composites. The characteristic peak (100) at 13.16° of g-C_3N_4 cannot be clearly observed in the XRD pattern of the heterojunction composites, which may be attributed to the decrease in the size of the lamellar structure caused by the stripping of bulk g-C_3N_4 into nanosheets [50].

In Fig. 4b, the FT-IR absorption spectra of HP-HKUST-1/g-C_3N_4 are displayed. It can be observed that HP-HKUST-1/g-C_3N_4 samples have six strong absorption peaks located at 1643 cm^{-1}, 1585 cm^{-1}, 1447 cm^{-1}, 1374 cm^{-1}, 808 cm^{-1} and 730 cm^{-1}. The absorption peaks at 1643 cm^{-1}, 1585 cm^{-1}, 1447 cm^{-1} and 1374 cm^{-1} belong to the symmetric and asymmetric vibrations of the carboxy groups in HKUST-1 [51]. The sharp peak at 808 cm^{-1} is attributed to the breathing vibration mode of tris-s-triazine units, and those strong bands in the 1200–1600 cm^{-1} region attributed to the stretching vibration of the C—N heterocycle [52]. The absorption peak at 730 cm^{-1} is a strong and sharp characteristic peak of Cu—O, which is attributed to the coordination bond formed between Cu^{2+} and the —COOH of H_3BTC in HKUST-1 [53]. And the broad peak around 3000–3500 cm^{-1} corresponds to the stretching vibration of N—H or hydroxyl groups in adsorbed water molecules [54].

Fig. 5 shows the X-ray photoelectron spectroscopy (XPS) reflecting the chemical composition and bonding characteristics of HP-HKUST-1/g-C_3N_4. The chemical structures corresponding to each peak in the XPS spectrum are summarized in Table 2.

The XPS survey spectrum of HP-HKUST-1/g-C_3N_4 (Fig. 5a) shows the photoelectron peaks featured in both g-C_3N_4 and HKUST-1, consistent with the EDS results (Fig. 2f). For the C 1s spectra (Fig. 5b) the two peaks associated with the C═O and C—O bonds in the carboxy group of HKUST-1 are not clearly resolved for the HP-HKUST-1/g-C_3N_4 sample, showing the effectiveness of the decarboxylation process [23]. The HP-HKUST-1/g-C_3N_4 C 1 s spectrum was dominated by the sp^2-hybridized carbon (N—C═N) in the nitrogen-containing aromatic rings of g-C_3N_4 and the C—C bond from the amorphous carbon of g-C_3N_4 and the benzine ring of the HKUST-1 [30,45,55]. The N 1 s spectrum (Fig. 5c) of HP-HKUST-1/g-C_3N_4 can be resolved into two peaks corresponding to that of tris-s-triazine units (C—N═C) and amino functional groups (C—N—H) on g-C_3N_4 [55], whilst the shake-up satellite owing to π electron excitation in g-C_3N_4 is not observed [56]. The O 1s spectrum of HP-HKUST-1/g-C_3N_4 shows the main peak featured in that of HKUST-1, but the O—H bond is not resolved, suggesting a decrease in water molecules adsorption to the surface of HKUST-1 [25] (Fig. 5d). For the Cu 2p spectra (Fig. 5e), HP-HKUST-1/g-C_3N_4 exhibits significantly reduced peak intensities for Cu(II) and its satellite compared to HKUST-1, while the Cu(I) peak shows marked enhancement, which is consistent with the decarboxylation process as the coordination bonds (Cu—O) in HP-HKUST-1/g-C_3N_4 are mostly broken, exposing more metal active sites and resulting in a significant increase in the content of Cu(I). This indicates a substantially higher Cu(I) proportion in HP-HKUST-1/g-C_3N_4. Furthermore, Cu LMM Auger spectra (Fig. S3, Supplementary materials) have been included to further elucidate the distribution of copper species in both materials. The peak intensity of Cu(I)/Cu(II) indicate that HKUST-1 is composed of Cu(II), while Cu(I) is the main component in the HP-HKUST-1/g-C_3N_4. The Cu LMM Auger analysis further confirms HP-HKUST-1/g-C_3N_4's elevated Cu(I) content versus HKUST-1, endowing it with superior reducing capability and enhanced Cu^{2+}/Cu^{+} interconversion that boosts ROS generation [21,57]. The valence band X-ray photoelectron spectra (VB-XPS) of HKUST-1 and g-C_3N_4 (Fig. 5f) allow the valence band edge to be determined for both materials. The valence band maxima (VBM) of g-C_3N_4 and the highest occupied orbital potential of HKUST-1 are determined to be 2.13 eV and

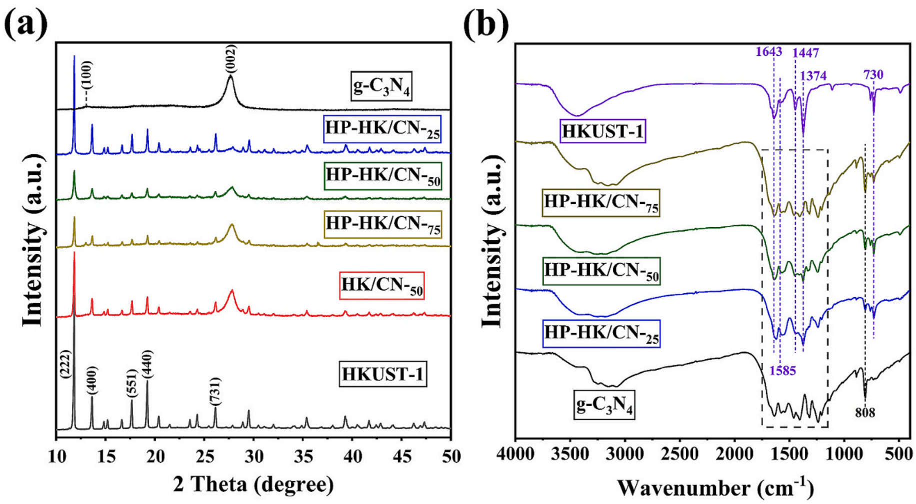

Fig. 4. (a) XRD spectra of g-C_3N_4, HKUST-1, HK/CN-$_{50}$ and HP-HK/CN-x; (b) FTIR spectra of g-C_3N_4, HKUST-1and HP-HK/CN-x.

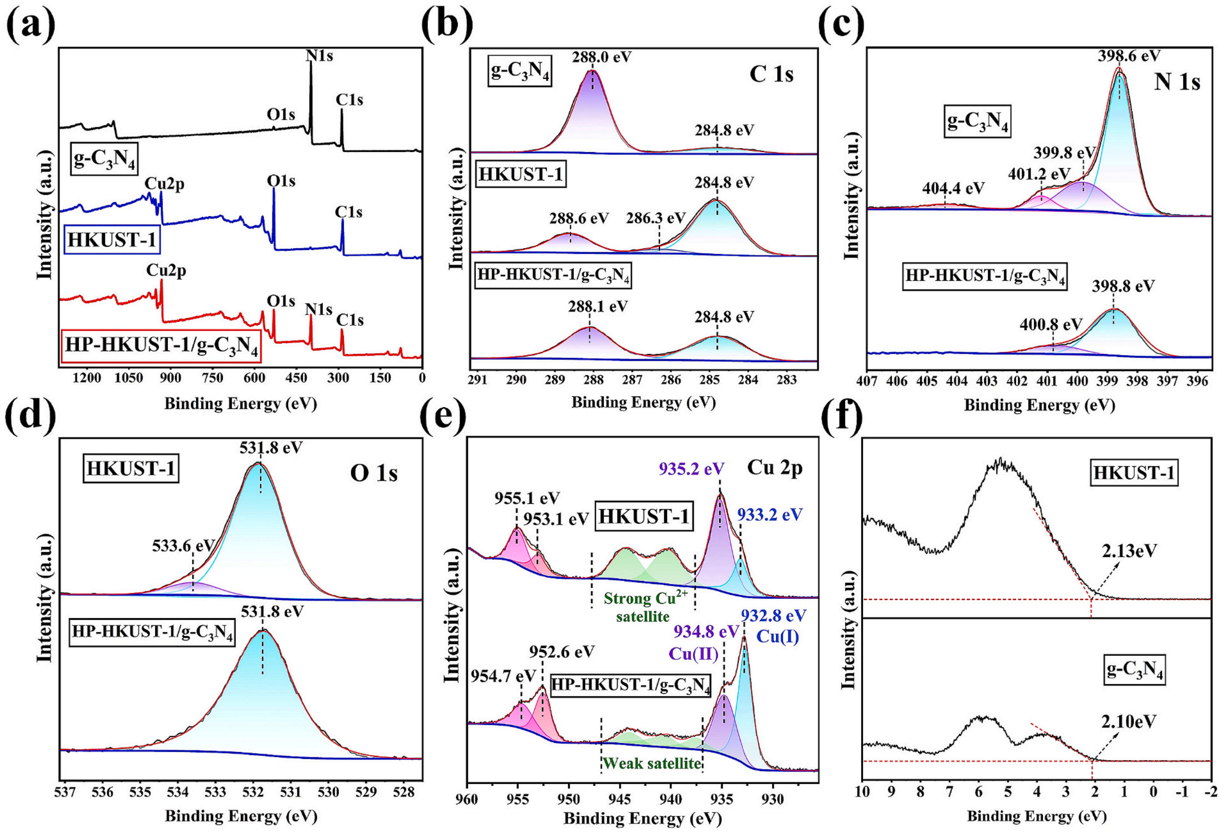

Fig. 5. Composition and bonding characteristics. (a) XPS spectra of g-C_3N_4, HKUST-1 and HP-HKUST-1/g-C_3N_4; (b) XPS C 1 s, (c) N 1 s, (d) O 1 s and (e) Cu 2p spectra; (f) Valence-band XPS spectra of g-C_3N_4 and HKUST-1. The g-C_3N_4 content in the HP-HKUST-1/g-C_3N_4 composite was 50 wt%.

Table 2
Photoelectron spectra binding energies and chemical states assigned for the samples g-C_3N_4, HKUST-1 and HP-HKUST-1/g-C_3N_4.

Peak	Binding energy (eV)	Chemical state
C 1s	284.8	C—C (from the amorphous carbon of g-C_3N_4) [55], C—C & C—H (from the sp^2-hybridized carbon of benzene rings of HKUST-1) [45]
	286.3	C-O (from the carboxy group of HKUST-1) [23]
	288.0, 288.1	N—C═N (from the sp^2-hybridized carbon of g-C_3N_4) [55]
	288.6	C═O (from the carboxy group of HKUST-1) [45]
N 1s	398.6, 398.8	C—N═C (from the tris-s-triazine units of g-C_3N_4) [55]
	399.8	N—C_3, H—N—C_2 (from the pyrrolic nitrogen of g-C_3N_4) [55]
	400.8, 401.2	C—N—H (from amino functional groups of g-C_3N_4) [55]
	404.4	the excitation of π electrons [56]
O 1s	531.8	adsorbed O_2 (from the HKUST-1) [23]
	533.6	O—H (from the adsorbed H_2O of HKUST-1) [23]
Cu 2p	932.8, 933.2, 952.6, 953.1	Cu(I) [57]
	934.8, 935.2, 954.7, 955.1	Cu(II) (from Cu-O coordination bond of HKUST-1) [57]
	936.0–947.0	Cu^{2+} satellite [57]

2.10 eV, respectively, indicating that g-C_3N_4 and HKUST-1 have similar valence band positions and comparable oxidation capabilities.

3.2. Optical and photoelectrochemical properties

Fig. 6 shows the ultraviolet–visible diffuse reflection spectrum (UV–vis DRS) and Photoluminescence (PL) spectra reflecting the photoresponse capability of HP-HKUST-1/g-C_3N_4. Fig. 6a displays the UV–vis DRS spectra of the samples. Compared with g-C_3N_4 and HKUST-1, the light absorption edge of HP-HKUST-1/g-C_3N_4 has a significant red shift, which might be attributed to the construction of heterojunction between g-C_3N_4 nanosheets and HKUST-1, leading to a change in band structure of the composite. The relationship between the absorption coefficient α and the incident photon energy, hν, is reflected by the Tauc formula [32]: $\alpha h\nu = A(h\nu - E_g)^{2/n}$, where E_g represents the bandgap and the constant n is determined by the semiconductor transition properties. The formula can be used to estimate the bandgap. As shown in Fig. 6b and c, the band gaps of g-C_3N_4, HKUST-1, HP-HK/CN-$_{25}$, HP-HK/CN-$_{50}$, and HP-HK/CN-$_{75}$ are 2.77 eV, 2.56 eV, 2.64 eV, 2.06 eV, and 2.63 eV, respectively. The band gap of HP-HK/CN-$_{50}$ (E_g = 2.06 eV) is much smaller than that of other samples, indicating that HP-HK/CN-$_{50}$ has the best photoresponse characteristics.

To investigate further the band structure of the HP-HK/CN-$_{50}$ heterojunction, both of the conduction band potential (E_{CB}) and valence band potential (E_{VB}) of g-C_3N_4 and the molecular orbital potential of HKUST-1 can be calculated with the following formula [58]: $E_{VB,NHE} = \varphi + E_{VB} - 4.44$; $E_{VB} = E_{CB} - E_g$, where φ represents the instrumental work function of XPS (e.g., 4.75 eV) and $E_{VB,XPS}$ is obtained from the VB-XPS spectrum (Fig. 5f). The E_{VB} and E_{CB} of g-C_3N_4 relative to the standard hydrogen electrode (NHE) were calculated to be 2.41 V and −0.36 V, respectively. And the highest occupied molecular orbital (HOMO) and lowest unoccupied molecular orbital (LUMO) potentials *vs* NHE of HKUST-1 were calculated to be 2.44 V and −0.12 V, respectively.

Fig. 6d shows the PL spectra of g-C_3N_4, HKUST-1 and HP-HK/CN-$_{50}$. Generally speaking, the separation efficiency of photogenerated carriers is negatively correlated with the intensity of PL [44]. In the PL spectra, strong peaks can be observed for g-C_3N_4 and HKUST-1 at 466 nm (with an excitation wavelength of 325 nm), which can be attributed to the recombination of electron-hole pairs. However, the PL spectrum of HP-HKUST-1/g-C_3N_4 shows a fluorescent quenching effect, and the

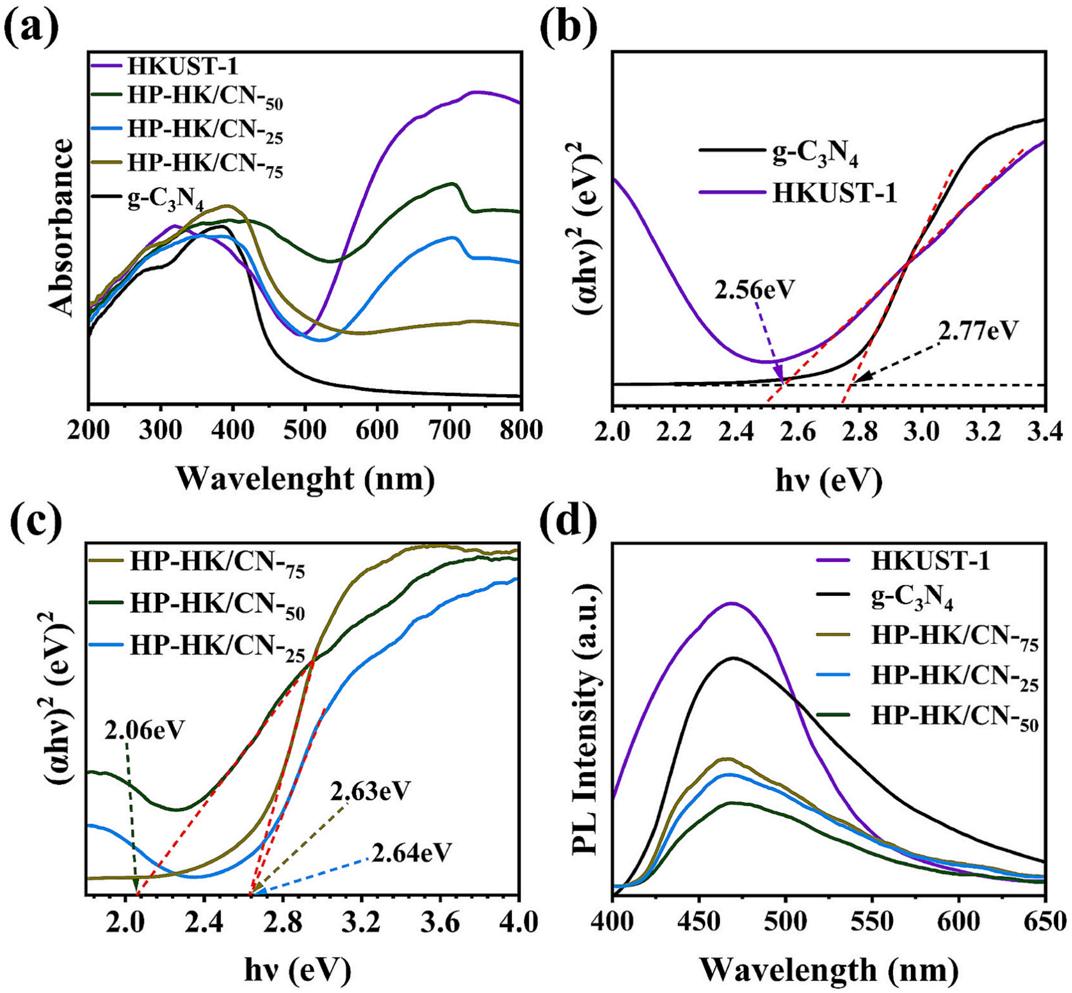

Fig. 6. (a) UV–vis DRS spectrum, (b) and (c) Tauc plots and (d) PL spectra of g-C_3N_4, HKUST-1 and HP-HKUST-1/g-C_3N_4.

fluorescence intensity of HP-HK/CN-$_{50}$ is weaker than that of g-C_3N_4, HKUST-1, HP-HK/CN-$_{25}$ and HP-HK/CN-$_{75}$, indicating that the heterojunction interface formed between g-C_3N_4 and HKUST-1 accelerates the transfer of photogenerated electrons, and the HP-HK/CN-$_{50}$ has excellent electron-hole separation capability.

To understand further the separation and recombination behavior of photogenerated carriers, the Electrochemical Impedance Spectroscopy (EIS) and transient photocurrent response curves of the composite materials were also investigated. Shown in Fig. 7a are the Electrochemical Impedance Spectroscopy (EIS) results. The Nyquist plots could be fitted with the simplified equivalent circuit model as shown in the inset of Fig. 7a. In the equivalent circuit, R_1 represents electrolyte ohmic resistance, R_2 represents the charge transfer resistance, which reflects the resistance to charge transfer between the electrode surface and reactants in the solution, CPE represents the constant phase element and W stand for Warburg element, respectively.

Relevant research has indicated that the smaller the arc diameter in the Nyquist plot, the smaller the charge transfer resistance (R_{ct}) at the semiconductor-electrolyte interface, and the higher the separation efficiency of photogenerated carriers and the interface charge transfer efficiency [31]. As shown in Fig. 7a, the arc radius of HP-HK/CN-$_{50}$ in the EIS spectrum is smaller than that of HKUST-1 and g-C_3N_4, indicating that HP-HK/CN-$_{50}$ can accelerate charge transfer through heterojunction. Fig. 7b shows the transient photocurrent response curves of g-C_3N_4, HKUST-1 and HP-HK/CN-$_{50}$. It can be seen that HP-HK/CN-$_{50}$ has the strongest photocurrent, indicating that HP-HK/CN-$_{50}$ has a higher photogenerated carrier separation efficiency and lifetime under light irradiation than that of the raw materials, namely, HKUST-1 and g-C_3N_4. Furthermore, HKUST-1 and HP-HK/CN-$_{50}$ exhibit relatively high dark current intensities, which is related to their strong reducing property.

In Fig. 7c, d, it can be observed that the tangent slopes of the Mott-Schottky curves of g-C_3N_4 and HKUST-1 are all positive, indicating that they have n-type semiconductor characteristics. Moreover, the flat band potentials (V_{fb}) of g-C_3N_4 and HKUST-1 relative to the Ag/AgCl electrode are −0.65 V and −0.42 V, respectively. Since the E_{CB} of the n-type semiconductor is usually 0.3 V smaller than the V_{fb} [59], thus the E_{CB} of g-C_3N_4 and E_{LUMO} of HKUST-1 are −0.95 V and −0.72 V, respectively. Based on the formula [60]: $E_{NHE} = E_{Ag/AgCl} + E^0_{Ag/AgCl} + 0.059 \times pH = E_{Ag/AgCl} + 0.61$ ($E^0_{Ag/AgCl} = 0.197$ V), the conduction band potential ($E_{CB,NHE}$) of g-C_3N_4 and the LUMO orbital potential ($E_{LUMO,NHE}$) of HKUST-1 are estimated to be −0.34 V and −0.11 V respectively, which are in general agreement with the previously determined values ($E_{CB,NHE} =$ −0.36 V, $E_{LUMO,NHE} =$ −0.12 V).

3.3. Catalytic degradation of tetracycline with and without illumination

Fig. 8 shows the TCH degradation performance of g-C_3N_4, HKUST-1, HK/CN-$_{50}$, HP-HK/CN-$_{25}$, HP-HK/CN-$_{50}$, and HP-HK/CN-$_{75}$ without and with visible illumination. As shown in Fig. 8a, the HP-HKUST-1/g-C_3N_4 composite catalysts can degrade TCH in a dark environment, and the degradation effect of the composites varies with the content and proportion of the original components. Furthermore, the HP-HK/CN-$_{50}$ has the best removal capacity in darkness.

Fig. 8b shows the degradation kinetic curves of HP-HK/CN-x, which

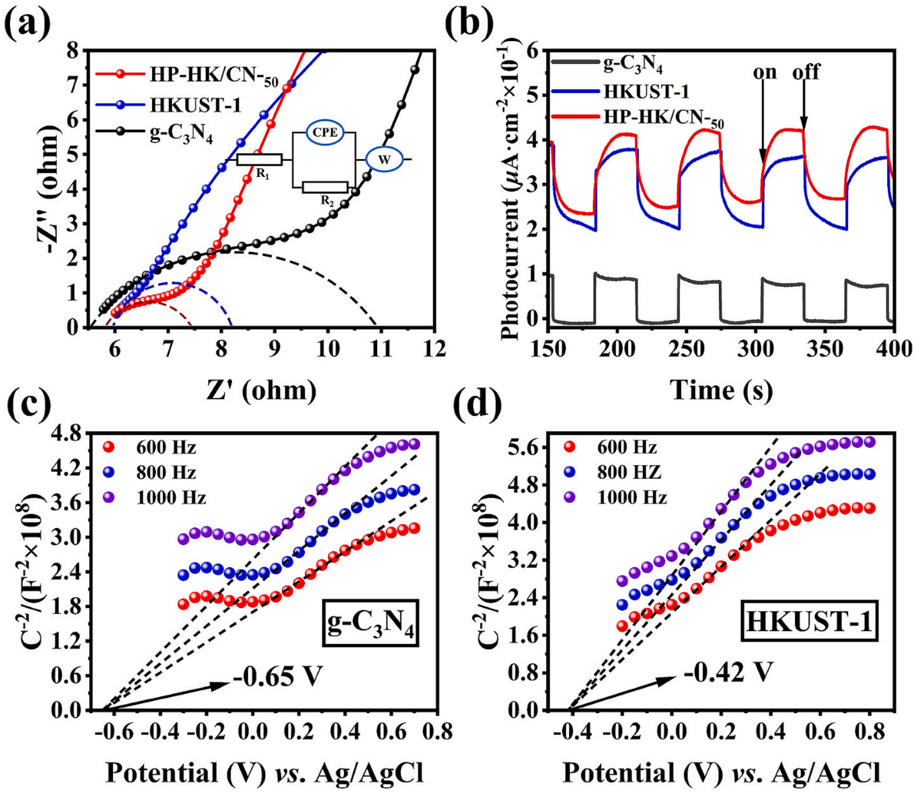

Fig. 7. (a) The Electrochemical impedance spectra shown as the Nyquist plots; (b) transient photocurrent responses of g-C_3N_4, HKUST-1 and that of HP-HK/CN-$_{50}$; (c) Mott-Schottky plots of g-C_3N_4 and (d) that of HKUST-1.

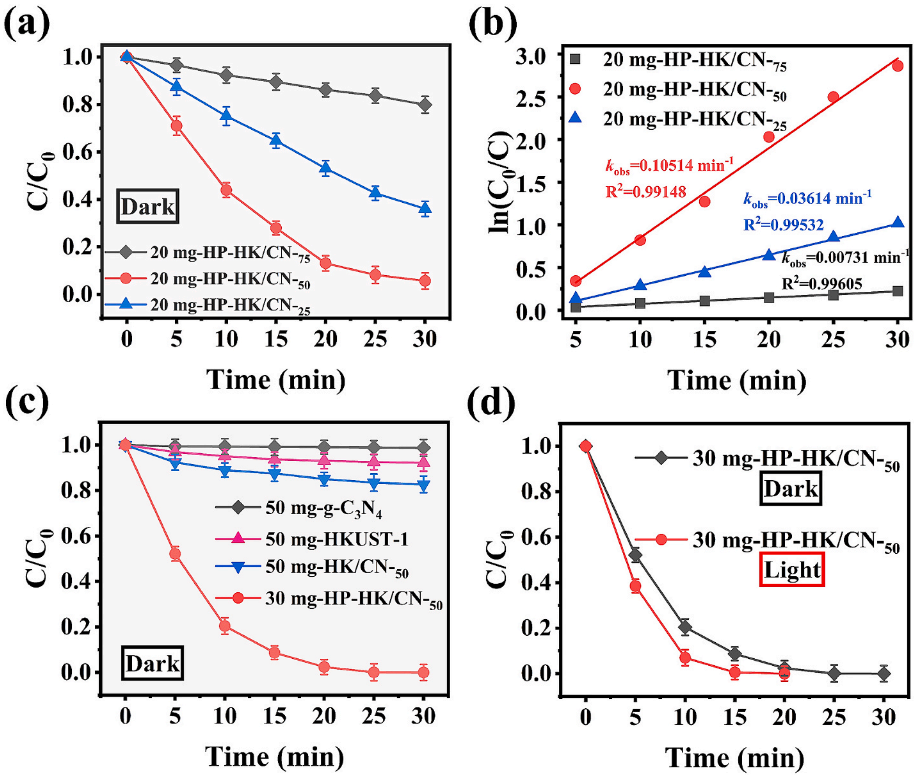

Fig. 8. (a) The degradation rate of TCH by 20 mg HP-HK/CN-x in the darkness; (b) The pseudo-first-order kinetics diagram of 20 mg HP-HK/CN-x; (c) The degradation rate of TCH by 50 mg g-C_3N_4, HKUST-1, HK/CN-$_{50}$ and 30 mg HP-HK/CN-$_{50}$ in the darkness; (d) The degradation rate of TCH by 30 mg HP-HK/CN-$_{50}$ in darkness and under visible illumination. Experimental condition: TCH quantity = 50 mL of 50 mg·L^{-1} concentration solution at 25 °C.

conform to the pseudo-first-order kinetic equation: $\ln(C_0/C) = kt$, where C_0 represents the initial TCH concentration and C represents the TCH concentration at time t [5]. It can be found that HP-HK/CN-$_{50}$ has the largest kinetic constant k value (0.10514 min^{-1}), which is about 14 times and 3 times that of HP-HK/CN-$_{75}$ (0.00731 min^{-1}) and HP-HK/CN-$_{25}$ (0.03614 min^{-1}), respectively. HP-HK/CN-$_{50}$ ($m_{HKUST\text{-}1}$: $m_{g\text{-}C_3N_4}$ = 1:1) has been shown to have the strongest catalytic ability to degrade TCH.

A comparison of the degradation efficiency of TCH in darkness (Fig. 8c) shows that 30 mg of HP-HK/CN-$_{50}$ achieved 99.92% degradation after 30 min, whereas 50 mg of g-C_3N_4, HKUST-1, and HK/CN-$_{50}$ show significantly lower efficiencies of 1.24%, 7.78%, and 17.36%, respectively.

In Fig. 8d, the degradation efficiencies are shown for 30 mg HP-HK/CN-$_{50}$ either in darkness or under visible illumination. Under visible illumination, the degradation efficiency of HP-HK/CN-$_{50}$ reached 99.95% within 20 min. To achieve similar degradation efficiency in darkness, an extra 10 min reaction time is required. HP-HK/CN-$_{50}$ exhibits the best performance in removing TCH, compared to MOF/g-C_3N_4 catalysts recently reported (see Table 3).

3.4. Degradation mechanism of HP-HKUST-1/g-C_3N_4

The excellent antibiotic degradation performance of HP-HKUST-1/g-C_3N_4 is mainly attributed to the following processes:

(A) The synergistic effects among micropores, mesopores, and macropores optimize the mass transfer efficiency of HP-HKUST-1/g-C_3N_4 and expose more Cu(I)/Cu(II) active sites. As shown in Fig. 9a-d, which are SEM images of HKUST-1 and HKUST-1/g-C_3N_4 after thermal treatment and decarboxylation, respectively, it can be clearly seen that after decarboxylation, HKUST-1 and HKUST-1/g-C_3N_4 formed a hierarchical porous structure, which is consistent with the result shown in Fig. 2d, indicating that the composite has a new kind of porous morphological structure after decarboxylation. Fig. 9e shows the decarboxylation process in HKUST-1, illustrating that during the decarboxylation, the coordination bonds and carboxyl groups in HKUST-1 are broken and peeled off, respectively, accompanied by the generation of CO_2 gas, thereby the original microporous structure is transformed into mesoporous as well as macroporous structures. Mesopores and macropores within hierarchical porous structure enhance mass transfer for storing and separating large molecules, whilst micropores make contributions to the high surface area and host–guest interactions [61]. Furthermore, the XPS results in Fig. 5e and Cu LMM Auger spectra in Fig. S3 (Supplementary materials) demonstrate that the decarboxylated composite achieves a higher Cu(I)/Cu(II) ratio by exposing more active sites. Thermodynamically, since the standard electrode potential of Cu^{2+}/Cu^+ (0.160 V *vs* NHE) is more negative than that of O_2/H_2O_2 (0.695 V *vs* NHE) [25], HP-HKUST-1/g-C_3N_4 can spontaneously reduce O_2 to H_2O_2 through electron transfer (Eq. (1) and Eq. (2)).

$$O_2(ads) + e^- \rightarrow \cdot O_2^- \tag{1}$$

$$\cdot O_2^- + e^- + 2H^+ \rightarrow H_2O_2 \tag{2}$$

(B) Owing to its superior reducing capability derived from the high Cu(I)/Cu(II) ratio, HP-HKUST-1/g-C_3N_4 can generate abundant ROS such as $\cdot OH$, $\cdot O_2^-$ and H_2O_2 through multiple pathways under dark conditions, which are used to efficiently remove TCH. The performance of HP-HKUST-1/g-C_3N_4 in generating active species in darkness can be verified by electron spin resonance (ESR) (Fig. 10). Both DMPO-$\cdot OH$ and DMPO-$\cdot O_2^-$ signals were detected (Fig. 10a, b) for the HKUST-1 and HP-HK/CN-$_{50}$ containing samples, and the intensity of the DMPO-$\cdot O_2^-$ signal corresponding to that of HP-HK/CN-$_{50}$ was much stronger than that of HKUST-1, whilst no signals were observed in the spectrum of g-C_3N_4. The ESR results demonstrate that the Cu(I) content is positively correlated with molecular oxygen activation capability. Compared to pristine HKUST-1, HP-HK/CN-$_{50}$ generates significantly more ROS.

In the darkness, the $\cdot OH$ and $\cdot O_2^-$ generated in HP-HK/CN-$_{50}$ can be produced through three pathways: the first is through the single-electron redox pathway (Eq. (1) and Eq. (3)); the second is the decomposition of H_2O_2 (Eq. (4)) and Eq. (5); the third is that H_2O_2 has a Fenton-like reaction with Cu^+ or Cu^{2+} to generate $\cdot O_2^-$ and $\cdot OH$ (Eq. (6) and Eq. (7)).

$$OH^- + e^- \rightarrow \cdot OH \tag{3}$$

$$H_2O_2 + e^- + H^+ \rightarrow \cdot OH + H_2O \tag{4}$$

$$H_2O_2 - e^- \rightarrow \cdot O_2^- + 2H^+ \tag{5}$$

$$Cu^+ + H_2O_2 \rightarrow Cu^{2+} + \cdot OH + OH^- \tag{6}$$

$$Cu^{2+} + H_2O_2 \rightarrow Cu^+ + \cdot O_2^- + 2H^+ \tag{7}$$

(C) Under visible illumination, HP-HKUST-1/g-C_3N_4 utilizes the interfacial effects of its heterojunction to enhance the transfer efficiency of photogenerated electrons, thereby promoting the single-electron reduction of O_2 and further improving the self-production efficiency of H_2O_2. The combined analysis of PL spectra (Fig. 6d), EIS spectra (Fig. 7a), and transient photocurrent responses (Fig. 7b) demonstrates that HP-HK/CN-$_{50}$ achieves

Table 3
Comparison of TCH degradation efficiency under visible illumination achieved by the reported MOF/g-C_3N_4-based photocatalysts.

Catalyst/Dosage ($g\cdot L^{-1}$)	C_0-TCH ($mg\cdot L^{-1}$) /Dosage (mL)	Time (Dark[d]/Light) (min)	1st cycle efficiency (%)	Degradation rate[e] ($mg_{TCH}\cdot g^{-1}\cdot min^{-1}$)	Ref
MOF-Co/g-C_3N_4 with PMS/0.2	20/250	30/60	90.20	1.00	[30]
Co/Mn-MOF-74@g-C_3N_4 with PMS/0.5	40/100	30/60	94.00	0.84	[31]
MOF-Fe/Co/boron-doped g-C_3N_4 with PS/0.3	60/50	30/40	97.50	2.79	[32]
Fe-based MOF@g-C_3N_4 with H_2O_2/0.5	40/100	30/60	92.00	0.82	[33]
MIL-Fe(53)/modified g-C_3N_4 with H_2O_2/0.375	30/80	30/60	100.00	0.89	[34]
(Zr/Ce)UiO-66(NH_2)@g-C_3N_4/0.2	10/100	60/120	98.00	0.27	[35]
HP-HKUST-1/g-C_3N_4/0.6	50/50	0[f]/20	99.95	4.16	this work

[d] The time of achieving adsorption–desorption equilibrium in darkness.

[e] The degradation rate is defined as the amount of TCH degraded per gram of catalyst per minute.

[f] HP-HKUST-1/g-C_3N_4 demonstrates efficient TCH degradation capability in darkness, thereby eliminating the necessity for adsorption–desorption equilibrium.

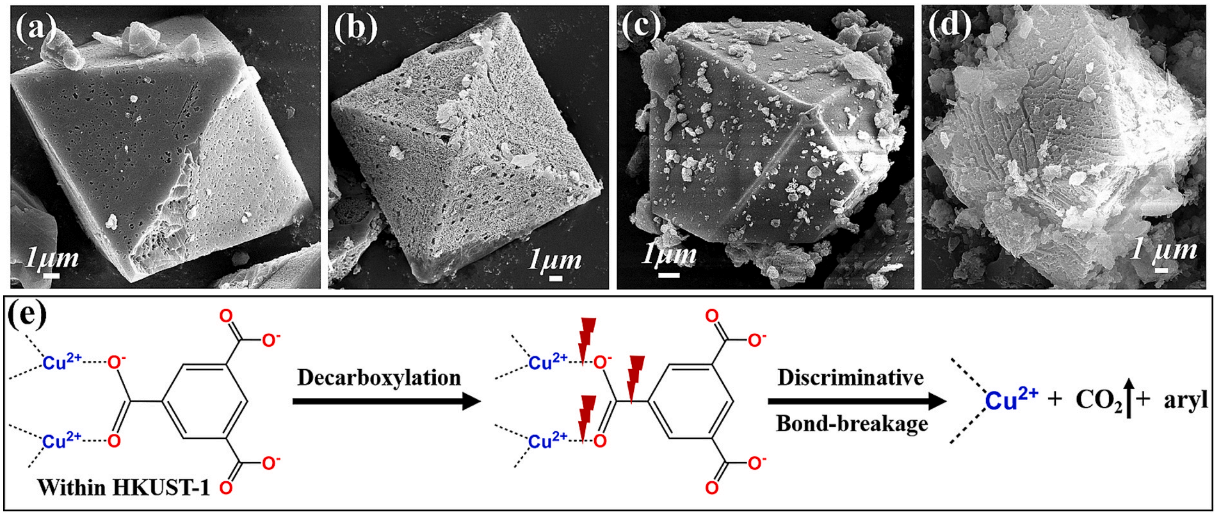

Fig. 9. (a-d) SEM images of (a) HKUST-1 with thermal treatment, (b) HKUST-1 with decarboxylation, (c) HKUST-1/g-C_3N_4 with thermal treatment and (d) HP-HKUST-1/g-C_3N_4; (e) Decarboxylation process within HKUST-1.

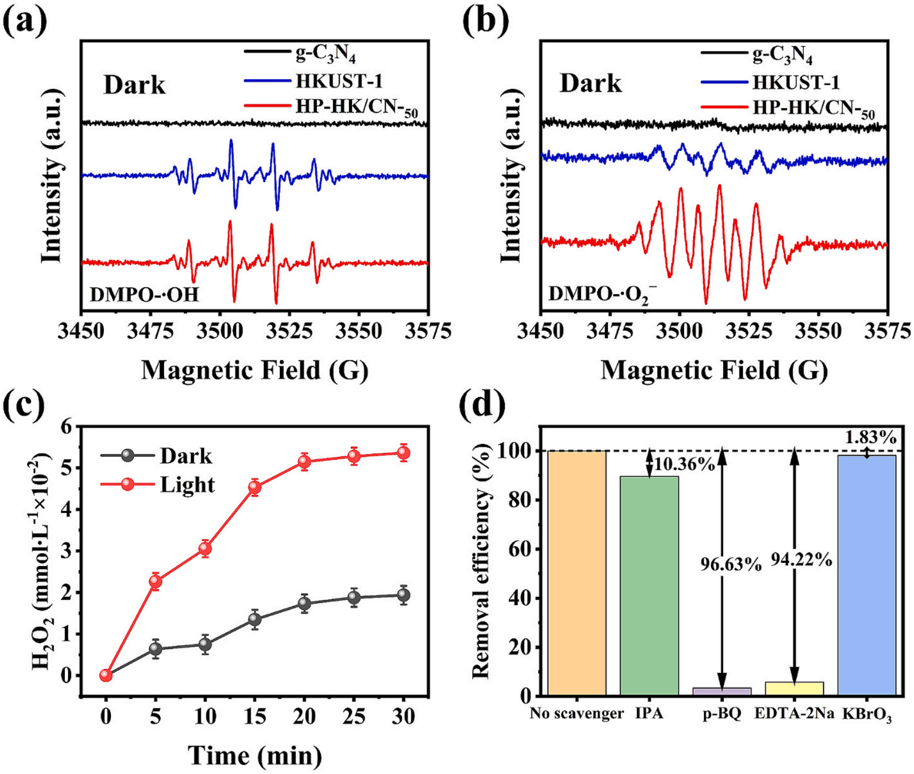

Fig. 10. (a-b) The ESR spectra of (a) DMPO-·OH signal and (b) DMPO-·O_2^- signal for g-C_3N_4, HKUST-1 and HP-HK/CN-$_{50}$ in darkness; (c) The yields of H_2O_2 using HP-HK/CN-$_{50}$ as catalyst in darkness and under visible illumination; (d) Reactive species trapping experiments of HP-HK/CN-$_{50}$ under visible illumination. Experiment conditions: [catalyst dosage] = 30 mg, 25 °C.

exceptional electron-hole separation efficiency and extended charge carrier lifetimes through heterojunction formation. This dual enhancement enables superior photocatalytic performance and facilitates photoelectron-assisted molecular oxygen activation. The catalytic performance of HP-HK/CN-$_{50}$ under visible illumination can be further evaluated by detecting the content of H_2O_2 and capturing the active species. It is worth noting that, as shown in Fig. 10c, the HP-HK/CN-$_{50}$ can detect H_2O_2 under both darkness and visible illumination, and the H_2O_2 concentration under visible illumination is higher than that in darkness. the reasons are that the photogenerated electrons produced by g-C_3N_4 can be transferred to the LUMO level of HKUST-1 through the heterojunction interface, which inhibits the recombination of photogenerated carriers in g-C_3N_4, and thus generating a large number of photogenerated holes for the degradation of TCH. Meanwhile, the valence state change between Cu^{2+} and Cu^{+} is accelerated by the photogenerated electrons migrating to HKUST-1from g-C_3N_4, providing sufficient electrons for the reduction of O_2 in HKUST-1, enhancing the efficiency of self-produced H_2O_2 and generating a large amount of ROS for the degradation of TCH.

As shown in Fig. 10d, to determine the main active species during the degradation of TCH by HP-HK/CN-$_{50}$ under visible illumination, IPA, p-BQ, EDTA-2Na and $KBrO_3$ were used to capture •OH, $•O_2^-$, h^+ and e^-, respectively. It can be seen that without a scavenger, the photocatalytic degradation efficiency of TCH by HP-HK/CN-$_{50}$ within 20 min is nearly 100%. When adding a certain amount of IPA and $KBrO_3$, the degradation efficiency of TCH only decreased by 10.36% and 1.83%, respectively, indicating that the influence of •OH and e^- on the degradation of TCH is relatively small; while after respectively adding an appropriate amount of p-BQ and EDTA-2Na, the degradation efficiency of TCH was significantly inhibited, inferring that the $•O_2^-$ and h^+ are the most dominant generated active species.

Fig. 11 is a schematic diagram illustrating the detailed mechanism of the synergistic effect between photocatalysis, molecular oxygen activation to produce H_2O_2 and Fenton-like reaction in the degradation of TCH of the HP-HK/CN-$_{50}$ system. As shown in Fig. 11, the band potentials of the composite material and its molecular oxygen activation performance under visible illumination elucidate the primary reactive species generation pathways during TCH degradation by HP-HK/CN-$_{50}$. On the one hand, since $E_{g(g\text{-}C3N4)} = 2.77$ eV, g-C_3N_4 can be excited by visible light ($\lambda > 420$ nm) to generate electron and hole pairs (Eq. (8)). The conduction band position of g-C_3N_4 ($E_{CB} = -0.36$ V *vs* NHE) is more negative than that of $O_2/•O_2^-$ (−0.33 V *vs* NHE), and g-C_3N_4 can theoretically generate $•O_2^-$ (Eq. (9)). However, the DMPO−$•O_2^-$ signal of g-C_3N_4 was not detected in darkness (Fig. 10b), so, g-C_3N_4 solely generates $•O_2^-$ through the reduction of O_2 by photogenerated electrons under visible illumination (Eq. (1)). On the other hand, the LUMO potential of HKUST-1 ($E_{LUMO} = -0.12$ V *vs* NHE) is higher than the redox potential of $O_2/•O_2^-$ (−0.33 V *vs* NHE), and thus HKUST-1 cannot theoretically reduce O_2 to $•O_2^-$. However, as shown in Fig. 10b, DMPO−$•O_2^-$ signals were indeed detected for both HKUST-1 and HP-HK/CN-$_{50}$, originating from three concurrent pathways: single-electron reduction of O_2 (Eq. (1)), decomposition of H_2O_2 (Eq. (5)), and Cu^{2+} mediated Fenton-like reactions with H_2O_2 (Eq. (7)). Moreover, the valence band potential of g-C_3N_4 ($E_{VB} = 2.41$ V *vs* NHE) and the HOMO potential of HKUST-1 ($E_{HOMO} = 2.44$ V *vs* NHE) are both greater than the redox potential of $H_2O/•OH$ (2.4 V *vs* NHE), indicating that g-C_3N_4 and HKUST-1 can thermodynamically oxidize H_2O to generate •OH. It can be inferred from above analysis that during the degradation process of TCH, a small amount of h^+ on the valence band of g-C_3N_4 and the HOMO orbital of HKUST-1 can react with H_2O/OH^- to generate •OH (Eq. (10)), while a large amount of h^+ directly degrades TCH.

$$g - C_3N_4 + h\nu \rightarrow h^+(g - C_3N_4) + e^-(g - C_3N_4) \tag{8}$$

$$O_2 + e^-(g - C_3N_4) \rightarrow \cdot O_2^- \tag{9}$$

$$H_2O/OH^- + h^+(HKUST - 1) \rightarrow \cdot OH \tag{10}$$

3.5. *Intermediates and degradation pathway of TCH*

To verify the degradation pathway and mechanism of HP-HK/CN-$_{50}$ to TCH, high performance liquid chromatography-mass spectrometry (HPLC-MS) System (SHIMADAZU, 20A, Japan) was used to detect the intermediate products during the degradation of TCH. The ionization mode is electrospray ionization with positive ion source (ESI +), and the mass-to-charge ratio (m/z) scanning range is 50 to 600. The results revealed that there are 17 major intermediates throughout the degradation process (please refer to Supplementary Material Fig. S5, Fig. S6 and Table S1, Supplementary materials). The mass spectrum of original TCH has a prominent peak at $m/z = 445$ [35], while the molecular ion peaks at $m/z = 149$, 290, 338 and 391 with the degradation effect of HP-HK/CN-$_{50}$ on TCH in darkness, which reveals that the •OH and $•O_2^-$ generated by the synergistic effect of molecular oxygen activation and Fenton-like reaction can degrade TCH. The appearance of smaller m/z (71, 97, 111, 114, and 121) indicates that HP-HK/CN-$_{50}$ can effectively degrade TCH into small molecules under visible illumination.

According to the m/z of the intermediate products, the possible degradation pathway of HP-HK/CN-$_{50}$ on TCH can be deduced, as shown in Fig. 12. In Pathway 1, TCH was attacked by •OH and $•O_2^-$ in darkness, and intermediates with $m/z = 432$, 413, and 391 were generated [62]. Subsequently, intermediates were gradually decomposed to produce species with $m/z = 290$, 149, 111 and 97 [63]. In Pathway 2, TCH was attacked by h^+ under visible illumination, forming the product with $m/z = 475$ [64]. In addition, the organic macromolecules were attacked by

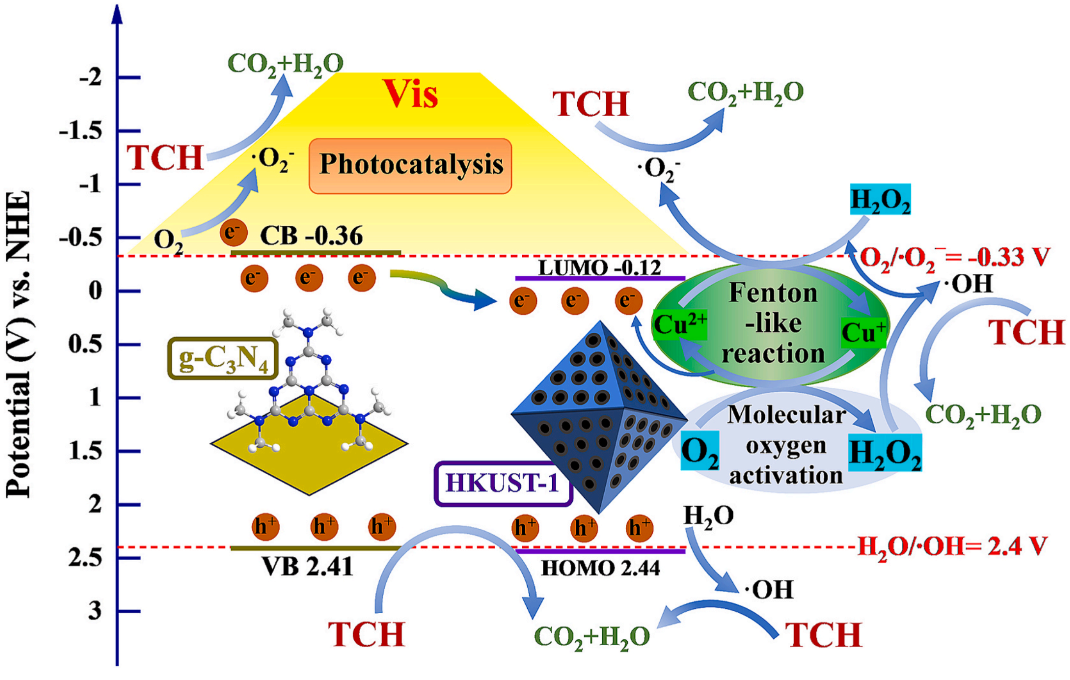

Fig. 11. The schematic diagram of mechanism of HP-HKUST-1/g-C_3N_4 degrading TCH under visible illumination.

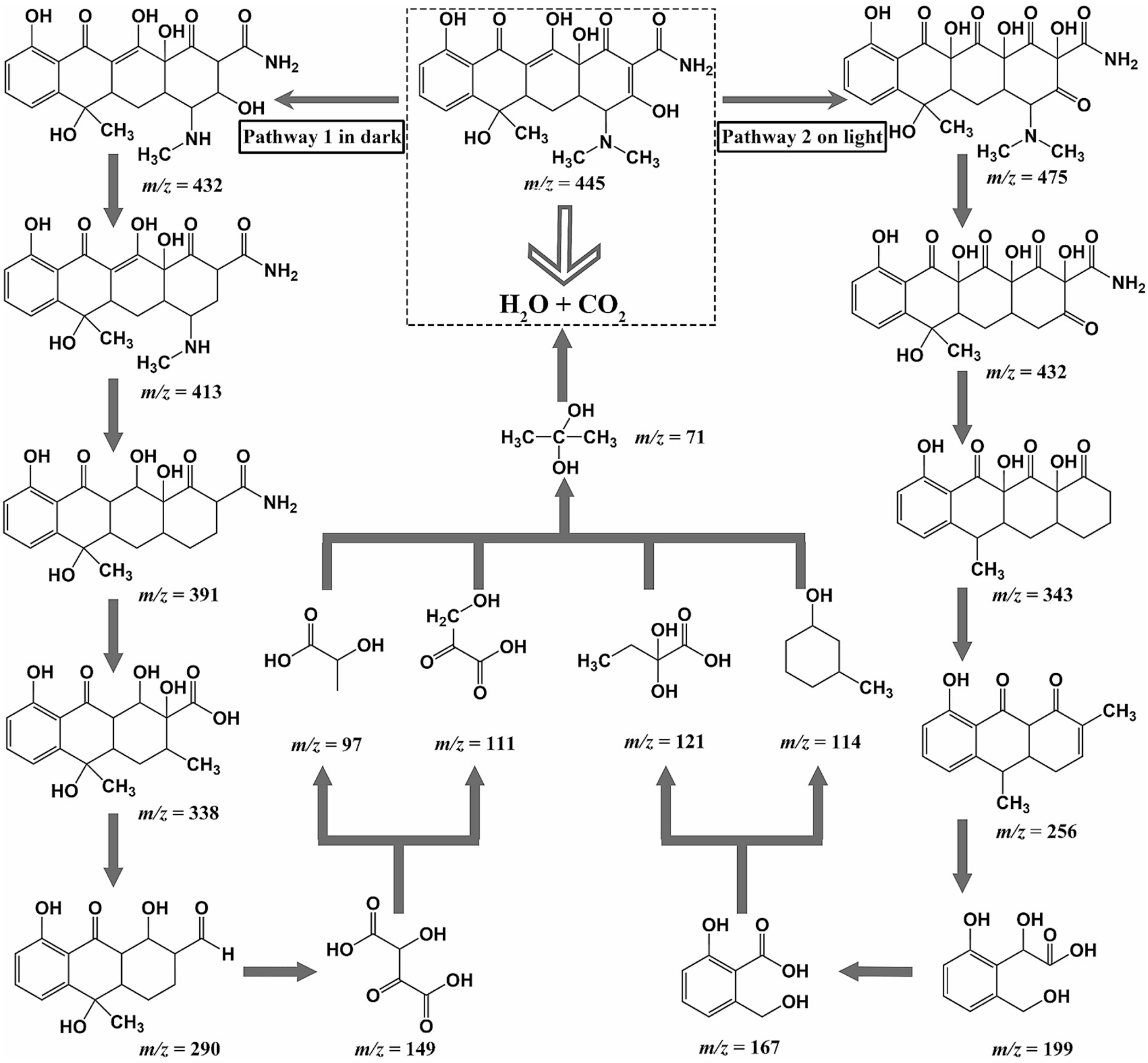

Fig. 12. The potential intermediates and degradation pathway of TCH in HP-HKUST-1/g-C_3N_4 system.

$\bullet O_2^-$, h^+, $\bullet OH$ and e^-, and gradually degraded into other small molecules (m/z = 432, 343, 256, 199, 167, 121, 114) [65]. Finally, the intermediates on both pathways were further decomposed by $\bullet O_2^-$, h^+, $\bullet OH$ and e^-, until they were transformed into CO_2 and H_2O.

3.6. Stability and reusability tests of HP-HKUST-1/g-C_3N_4

Stability and reusability are critical metrics for evaluating the practical potential of catalysts. Based on the studies, HP-HK/CN-$_{50}$ was subjected to three consecutive TCH degradation cycles under light irradiation. After three cycles, the photocatalytic efficiency decreased by approximately 23% (Fig. 13a). To elucidate the possible reasons for the decline in degradation efficiency and further validate the catalyst's stability, post-catalytic HP-HK/CN-$_{50}$ was collected after three cycles for structural characterization. As shown in Fig. 13b and c, the XRD and FT-IR spectra of HP-HK/CN-$_{50}$ before and after use remained highly consistent, with no significant shifts in peak positions, indicating that the catalyst's crystal structure and elemental composition were preserved. SEM images (Fig. S7b, Supplementary materials) of HP-HK/CN-$_{50}$ after 60 min of cycling confirmed that the catalyst's morphology remained intact, whereas non-decarboxylated HK/CN-$_{50}$ underwent severe hydrolysis and structural collapse during use.

Furthermore, Fig. 13d clearly shows a decrease in the intensity of the Cu(I) peak and an increase in the Cu^{2+} satellite peak for post-reaction HP-HK/CN-$_{50}$, demonstrating a reduction in Cu(I) content and a corresponding rise in Cu(II) proportion. This shift weakened the composite's reducing capacity, as the catalytic process continuously consumed Cu^+ to activate O_2 for H_2O_2 generation. The limited regeneration of Cu^+ via photogenerated electrons disrupted the Cu^+/Cu^{2+} dynamic equilibrium, ultimately leading to the decline in Cu(I) content. Furthermore, ICP-MS analysis of the post-reaction solution revealed a copper concentration of 2.55 mg/L, corresponding to a leaching rate of 2.9%. This reflects the consumption of Cu(I)/Cu(II) species during the degradation process. In summary, HP-HK/CN-$_{50}$ exhibits excellent structural stability, and its catalytic activity is directly proportional to the Cu(I) content.

4. Conclusions

A hierarchical porous heterojunction catalyst, HP-HKUST-1/g-C_3N_4, composed of semiconducting g-C_3N_4 and copper-based metal–organic framework, HKUST-1, has been designed and synthesized through electrostatic self-assembly, hydrothermal synthesis and decarboxylation. We have demonstrated that HP-HK/CN-$_{50}$ has an enhanced catalytic effect on the degradation of tetracycline hydrochloride under total

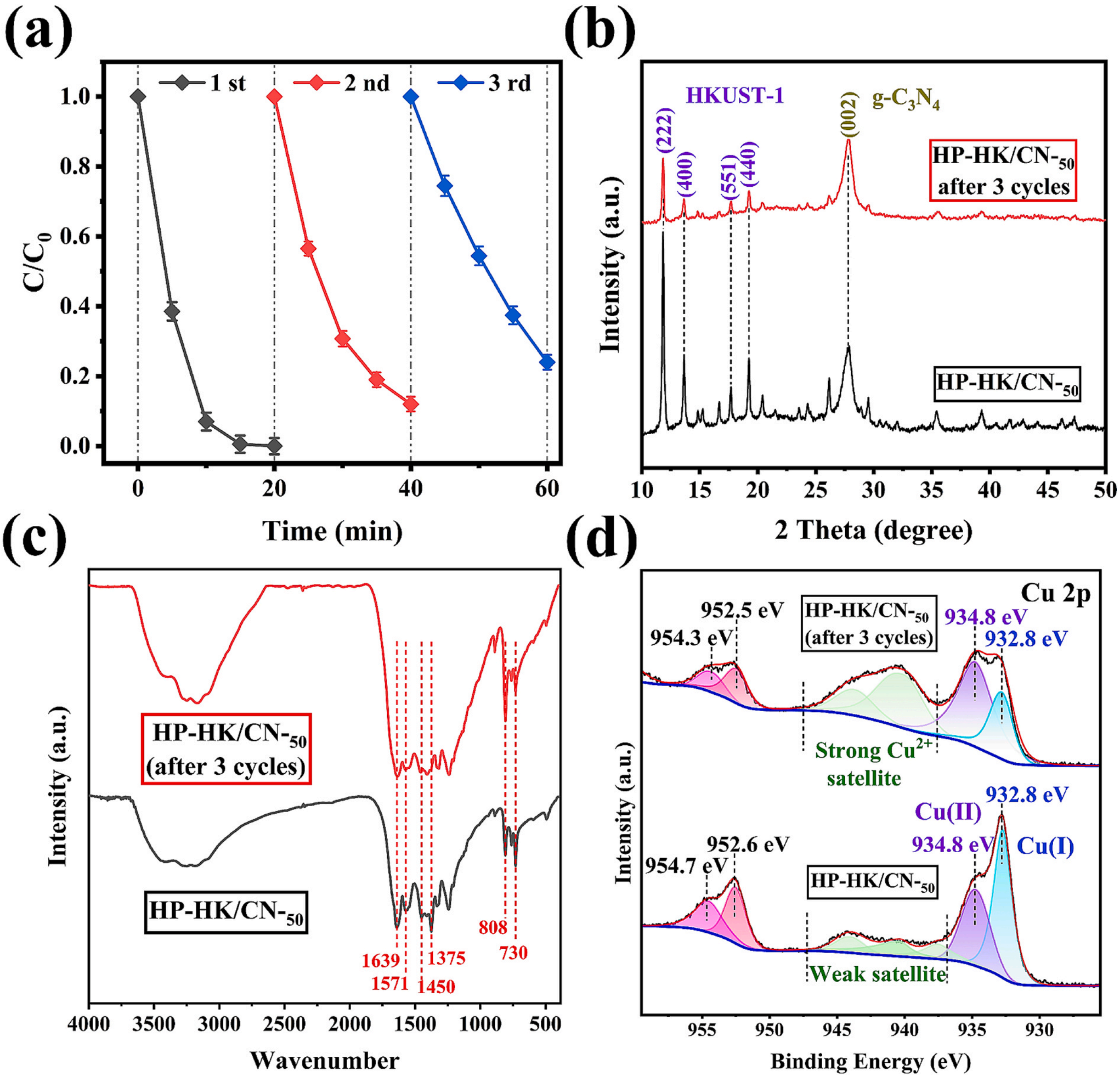

Fig. 13. (a) Cyclic stability tests of HP-HK/CN-$_{50}$ photocatalytic degradation of TCH; (b) XRD, (c) FT-IR and (d) XPS Cu 2p spectra of HP-HK/CN-$_{50}$ before experiment and after 3 photocatalysis cycles.

darkness, and more, its catalytic effect is further increased under the visible illumination. HP-HK/CN-$_{50}$ has been shown, without any externally provided oxidants and in darkness, to exhibit a superb TCH degradation efficiency of 99.92% over 30 min. Under visible illumination, it reaches to an efficiency of 99.95% within ~20 min, far exceeding those comparable catalysts reported under similar conditions (see Table 3).

The excellent catalytic performance of HP-HK/CN-$_{50}$ is attributed to its high Cu(I)/Cu(II) ratio, which facilitates single-electron transfer to activate molecular oxygen for spontaneous H_2O_2 generation, thereby overcoming the limitations of external oxidant supply and illumination dependency. The effective electron transfer at the interface of the heterojunctions between HKUST-1 and g-C_3N_4 further improves the separation of photogenerated carriers, enhancing the catalytic performance under illumination, and enabling efficient synergies among molecular oxygen activation, photocatalysis and Fenton-like reactions. In addition, the great stability of HP-HK/CN-$_{50}$ was shown by three runs' cycle experiment. The work demonstrates the practical potential of such catalysts and their future variations in wastewater treatment as an efficient technique with molecular oxygen activation properties for the removal of antibiotics.

CRediT authorship contribution statement

Liqin Nie: Writing – original draft, Validation, Investigation, Formal analysis, Conceptualization. **Kaige Wang:** Writing – review & editing, Writing – original draft, Supervision, Resources, Project administration, Methodology, Funding acquisition, Formal analysis, Conceptualization. **Wei Zhao:** Writing – review & editing, Supervision, Resources, Data curation. **Chen Zhang:** Writing – review & editing, Supervision, Resources, Methodology, Data curation. **Tiehan Shen:** Writing – review & editing, Writing – original draft, Supervision, Methodology, Formal analysis, Conceptualization.

Declaration of competing interest

The authors declare that they have no known competing financial interests or personal relationships that could have appeared to influence the work reported in this paper.

Acknowledgements

This research was supported by the National Natural Science Foundation of China (Nos. 62275216, 61775181), the Natural Science Basic Research Program of Shaanxi Province-Major Basic Research Project (Nos. S2018-ZC-TD-0061, TZ0393), and the National Key Scientific Instrument and Equipment Development Projects of China (No. 51927804). Authors would like to thank Dr. Yi Wang and Dr. Shenghua Ma for their helpful discussions on degradation mechanism and paper writing.

Appendix A. Supplementary data

Supplementary data to this article can be found online at https://doi.org/10.1016/j.seppur.2025.133894.

Data availability

Data will be made available on request.

References

[1] L. Xu, H. Zhang, P. Xiong, Q. Zhu, C. Liao, G. Jiang, Occurrence, fate, and risk assessment of typical tetracycline antibiotics in the aquatic environment: a review, Sci. Total Environ. 753 (2021) 141975, https://doi.org/10.1016/j.scitotenv.2020.141975.

[2] X. Zhang, T. Cai, S. Zhang, J. Hou, L. Cheng, W. Chen, Q. Zhang, Contamination distribution and non-biological removal pathways of typical tetracycline antibiotics in the environment: a review, J. Hazard. Mater. 463 (2023) 132862, https://doi.org/10.1016/j.jhazmat.2023.132862.

[3] K. Wang, T. Zhuang, Z. Su, M. Chi, H. Wang, Antibiotic residues in wastewaters from sewage treatment plants and pharmaceutical industries: occurrence, removal and environmental impacts, Sci. Total Environ. 788 (2021) 147811, https://doi.org/10.1016/j.scitotenv.2021.147811.

[4] A. Mann, K. Nehra, J.S. Rana, T. Dahiya, Antibiotic resistance in agriculture: perspectives on upcoming strategies to overcome upsurge in resistance, Curr. Res. Microb. Sci. 2 (2021) 100030, https://doi.org/10.1016/j.crmicr.2021.100030.

[5] T. Gao, H. Zhang, X. Zhao, S. Xiao, Z. Zhang, S. Yu, Efficient removal of tetracycline from MOF-on-MOF heterojunctions driven by visible light: evaluation of photocatalytic mechanisms and degradation pathway, Appl. Surf. Sci. 651 (2024) 159227, https://doi.org/10.1016/j.apsusc.2023.159227.

[6] J. Jiang, X. Wang, C. Yue, S. Liu, Y. Lin, T. Xie, S. Dong, Efficient photoactivation of peroxymonosulfate by Z-scheme nitrogen-defect-rich $NiCo_2O_4$/g-C_3N_4 for rapid emerging pollutants degradation, J. Hazard. Mater. 414 (2021) 125528, https://doi.org/10.1016/j.jhazmat.2021.125528.

[7] M. Zhang, Y.S. Liu, J.L. Zhao, W.R. Liu, L.Y. He, J.N. Zhang, J. Chen, L.K. He, Q. Q. Zhang, G.G. Ying, Occurrence, fate and mass loadings of antibiotics in two swine wastewater treatment systems, Sci. Total Environ. 639 (2018) 1421–1431, https://doi.org/10.1016/j.scitotenv.2018.05.230.

[8] C.Y. Ren, Q.J. Xu, P.J.J. Alvarez, L. Zhu, H.P. Zhao, Simultaneous antibiotic removal and mitigation of resistance induction by manganese bio-oxidation process, Water Res. 244 (2023) 120442, https://doi.org/10.1016/j.watres.2023.120442.

[9] L. Zhu, L. Yuan, X.Y. Shuai, Z.J. Lin, Y.J. Sun, Z.C. Zhou, L.X. Meng, F. Ju, H. Chen, Deciphering basic and key traits of antibiotic resistome in influent and effluent of hospital wastewater treatment systems, Water Res. 231 (2023) 119614, https://doi.org/10.1016/j.watres.2023.119614.

[10] D. Wang, F. Jia, H. Wang, F. Chen, Y. Fang, W. Dong, G. Zeng, X. Li, Q. Yang, X. Yuan, Simultaneously efficient adsorption and photocatalytic degradation of tetracycline by Fe-based MOFs, J. Colloid Interface Sci. 519 (2018) 273–284, https://doi.org/10.1016/j.jcis.2018.02.067.

[11] J. Scaria, K.V. Anupama, P.V. Nidheesh, Tetracyclines in the environment: an overview on the occurrence, fate, toxicity, detection, removal methods, and sludge management, Sci. Total Environ. 771 (2021) 145291, https://doi.org/10.1016/j.scitotenv.2021.145291.

[12] N. Lu, F. Liu, Tempospatially confined catalytic membranes for advanced water remediation, Adv. Mater. 36 (2024) 2311419, https://doi.org/10.1002/adma.202311419.

[13] X.-H. Yi, T.-Y. Wang, H.-Y. Chu, Y. Gao, C.-C. Wang, Y.-J. Li, L. Chen, P. Wang, H. Fu, C. Zhao, W. Liu, Effective elimination of tetracycline antibiotics via photoactivated SR-AOP over vivianite: a new application approach of phosphorus recovery product from WWTP, Chem. Eng. J. 449 (2022) 137784, https://doi.org/10.1016/j.cej.2022.137784.

[14] Y.J. Zhang, G.X. Huang, L.R. Winter, J.J. Chen, L. Tian, S.C. Mei, Z. Zhang, F. Chen, Z.Y. Guo, R. Ji, Y.Z. You, W.W. Li, X.W. Liu, H.Q. Yu, M. Elimelech, Simultaneous nanocatalytic surface activation of pollutants and oxidants for highly efficient water decontamination, Nat. Commun. 13 (2022) 3005, https://doi.org/10.1038/s41467-022-30560-9.

[15] Y. Wang, H. Song, J. Chen, S. Chai, L. Shi, C. Chen, Y. Wang, C. He, A novel solar photo-Fenton system with self-synthesizing H_2O_2: enhanced photo-induced catalytic performances and mechanism insights, Appl. Surf. Sci. 512 (2020) 145650, https://doi.org/10.1016/j.apsusc.2020.145650.

[16] J. Yang, M. Zhu, D.D. Dionysiou, What is the role of light in persulfate-based advanced oxidation for water treatment? Water Res. 189 (2021) 116627 https://doi.org/10.1016/j.watres.2020.116627.

[17] Q. Bi, Y. Zhao, B. Yang, Y. Du, Y. Xue, K. Zhang, J. Xue, Activation of H_2O_2 using a single-atom Cu catalyst for efficient tetracycline degradation, Appl. Surf. Sci. 676 (2024) 160943, https://doi.org/10.1016/j.apsusc.2024.160943.

[18] Z. Yang, J. Wang, Photo-Fenton degradation of sulfamethazine using self-assembled CdS nanorods with in-situ production of H_2O_2 at wide pH range, Chem. Eng. J. 450 (2022) 138024, https://doi.org/10.1016/j.cej.2022.138024.

[19] Y. Chen, Y. Liu, X. Gong, J. Wang, Photocatalytic degradation of chlorinated organic pollutants by ZnS@ZIF-8 composite through hydrogen peroxide generation by activating dioxygen under simulated sunlight irradiation, J. Colloid Interface Sci. 654 (2024) 1417–1430, https://doi.org/10.1016/j.jcis.2023.10.156.

[20] N.T. Vo, Y. Mekmouche, T. Tron, R. Guillot, F. Banse, Z. Halime, M. Sircoglou, W. Leibl, A. Aukauloo, A reversible electron relay to exclude sacrificial electron donors in the photocatalytic oxygen atom transfer reaction with O_2 in water, Angew. Chem., Int. Ed. 58 (2019) 16023–16027, https://doi.org/10.1002/anie.201907337.

[21] G. Dong, Z. Ai, L. Zhang, Total aerobic destruction of azo contaminants with nanoscale zero-valent copper at neutral pH: promotion effect of in-situ generated carbon center radicals, Water Res. 66 (2014) 22–30, https://doi.org/10.1016/j.watres.2014.08.011.

[22] M. Stefaniuk, P. Oleszczuk, Y.S. Ok, Review on nano zerovalent iron (nZVI): from synthesis to environmental applications, Chem. Eng. J. 287 (2016) 618–632, https://doi.org/10.1016/j.cej.2015.11.046.

[23] L. Yuan, Z. Wang, F. Gu, Efficient degradation of tetracycline hydrochloride by direct Z-scheme HKUST-1@m-$BiVO_4$ catalysts with self-produced H_2O_2 under both dark and light, J. Environ. Chem. Eng. 10 (2022) 107964, https://doi.org/10.1016/j.jece.2022.107964.

[24] W. Wang, D.I. Sharapa, A. Chandresh, A. Nefedov, S. Heissler, L. Heinke, F. Studt, Y. Wang, C. Woll, Interplay of electronic and steric effects to yield low-temperature CO oxidation at metal single sites in defect-engineered HKUST-1, Angew. Chem., Int. Ed. 59 (2020) 10514–10518, https://doi.org/10.1002/anie.202000385.

[25] F. Zhang, G. Dong, M. Wang, Y. Zeng, C. Wang, Efficient removal of methyl orange using Cu_2O as a dual function catalyst, Appl. Surf. Sci. 444 (2018) 559–568, https://doi.org/10.1016/j.apsusc.2018.03.087.

[26] Y. Li, Y. Fang, Z. Cao, N. Li, D. Chen, Q. Xu, J. Lu, Construction of g-C_3N_4/PDI@MOF heterojunctions for the highly efficient visible light-driven degradation of pharmaceutical and phenolic micropollutants, Appl. Catal. B Environ. 250 (2019) 150–162, https://doi.org/10.1016/j.apcatb.2019.03.024.

[27] G. Zhang, D. Huang, M. Cheng, L. Lei, S. Chen, R. Wang, W. Xue, Y. Liu, Y. Chen, Z. Li, Megamerger of MOFs and g-C_3N_4 for energy and environment applications: upgrading the framework stability and performance, J. Mater. Chem. A 8 (2020) 17883–17906, https://doi.org/10.1039/d0ta05662f.

[28] F. Wang, J. Xu, Z. Wang, Y. Lou, C. Pan, Y. Zhu, Unprecedentedly efficient mineralization performance of photocatalysis-self-Fenton system towards organic pollutants over oxygen-doped porous g-C_3N_4 nanosheets, Appl. Catal. B Environ. 312 (2022) 121438, https://doi.org/10.1016/j.apcatb.2022.121438.

[29] L. Tian, X. Yang, Q. Liu, F. Qu, H. Tang, Anchoring metal-organic framework nanoparticles on graphitic carbon nitrides for solar-driven photocatalytic hydrogen evolution, Appl. Surf. Sci. 455 (2018) 403–409, https://doi.org/10.1016/j.apsusc.2018.06.014.

[30] C. Jin, M. Wang, Z. Li, J. Kang, Y. Zhao, J. Han, Z. Wu, Two dimensional Co_3O_4/g-C_3N_4 Z-scheme heterojunction: mechanism insight into enhanced peroxymonosulfate-mediated visible light photocatalytic performance, Chem. Eng. J. 398 (2020) 125569, https://doi.org/10.1016/j.cej.2020.125569.

[31] Q. Wen, D. Li, H. Li, M. Long, C. Gao, L. Wu, F. Song, J. Zhou, Synergetic effect of photocatalysis and peroxymonosulfate activated by Co/Mn-MOF-74@g-C_3N_4 Z-scheme photocatalyst for removal of tetracycline hydrochloride, Sep. Purif. Technol. 313 (2023) 123518, https://doi.org/10.1016/j.seppur.2023.123518.

[32] J. Li, H. Wang, N. Reddy, Z. Zhu, J. Zheng, W. Wang, B. Liu, C. Hu, MOF_{FeCo}/B-CN composites achieve efficient degradation of antibiotics in a non-homogeneous concurrent photocatalytic-persulfate activation system, Sci. Total Environ. 858 (2023) 159795, https://doi.org/10.1016/j.scitotenv.2022.159795.

[33] T. Guo, K. Wang, G. Zhang, X. Wu, A novel α-Fe_2O_3@g-C_3N_4 catalyst: synthesis derived from Fe-based MOF and its superior photo-Fenton performance, Appl. Surf. Sci. 469 (2019) 331–339, https://doi.org/10.1016/j.apsusc.2018.10.183.

[34] Y. Pan, X. Hu, M. Bao, F. Li, Y. Li, J. Lu, Fabrication of MIL-Fe (53)/modified g-C_3N_4 photocatalyst synergy H_2O_2 for degradation of tetracycline, Sep. Purif. Technol. 279 (2021) 119661, https://doi.org/10.1016/j.seppur.2021.119661.

[35] S. Ren, J. Dong, X. Duan, T. Cao, H. Yu, Y. Lu, D. Zhou, A novel (Zr/Ce)UiO-66 (NH_2)@g-C_3N_4 Z-scheme heterojunction for boosted tetracycline photodegradation via effective electron transfer, Chem. Eng. J. 460 (2023) 141884, https://doi.org/10.1016/j.cej.2023.141884.

[36] P. Niu, L. Zhang, G. Liu, H.M. Cheng, Graphene-Like carbon nitride nanosheets for improved photocatalytic activities, Adv. Funct. Mater. 22 (2012) 4763–4770, https://doi.org/10.1002/adfm.201200922.

[37] S. Yang, Y. Gong, J. Zhang, L. Zhan, L. Ma, Z. Fang, R. Vajtai, X. Wang, P. M. Ajayan, Exfoliated graphitic carbon nitride nanosheets as efficient catalysts for hydrogen evolution under visible light, Adv. Mater. 25 (2013) 2452–2456, https://doi.org/10.1002/adma.201204453.

[38] X. Lu, K. Xu, P. Chen, K. Jia, S. Liu, C. Wu, Facile one step method realizing scalable production of g-C_3N_4 nanosheets and study of their photocatalytic H_2 evolution activity, J. Mater. Chem. A 2 (2014) 18924–18928, https://doi.org/10.1039/c4ta04487h.

[39] S. Zhang, Y. Shen, J. Lu, Z. Chen, L. Li, F. Guo, W. Shi, Tannic acid-modified g-C_3N_4 nanosheets/polydimethylsiloxane as a photothermal-responsive self-healing composite coating for smart corrosion protection, Chem. Eng. J. 483 (2024) 149232, https://doi.org/10.1016/j.cej.2024.149232.

[40] J. Cai, J. Huang, S. Wang, J. Iocozzia, Z. Sun, J. Sun, Y. Yang, Y. Lai, Z. Lin, Crafting mussel-inspired metal Nanoparticle-decorated ultrathin graphitic carbon nitride for the degradation of chemical pollutants and production of chemical resources, Adv. Mater. 31 (2019) 1806314, https://doi.org/10.1002/adma.201806314.

[41] L. Shi, T. Wang, H. Zhang, K. Chang, J. Ye, Electrostatic self-assembly of nanosized Carbon nitride nanosheet onto a zirconium metal–organic framework for enhanced photocatalytic CO_2 reduction, Adv. Funct. Mater. 25 (2015) 5360–5367, https://doi.org/10.1002/adfm.201502253.

[42] X. Ma, L. Wang, H. Wang, J. Deng, Y. Song, Q. Li, X. Li, A.M. Dietrich, Insights into metal-organic frameworks HKUST-1 adsorption performance for natural organic matter removal from aqueous solution, J. Hazard. Mater. 424 (2022) 126918, https://doi.org/10.1016/j.jhazmat.2021.126918.

[43] C. Feng, L. Tang, Y. Deng, J. Wang, J. Luo, Y. Liu, X. Ouyang, H. Yang, J. Yu, J. Wang, Synthesis of leaf-vein-like g-C_3N_4 with tunable band structures and charge transfer properties for selective photocatalytic H_2O_2 evolution, Adv. Funct. Mater. 30 (2020) 2001922, https://doi.org/10.1002/adfm.202001922.

[44] Y. Qiao, C. Sun, J. Jian, T. Zhou, X. Xue, J. Shi, G. Che, G. Liao, Efficient removal of organic pollution via photocatalytic degradation over a TiO_2@HKUST-1 yolk-shell nanoreactor, J. Mol. Liq. 385 (2023) 122383, https://doi.org/10.1016/j.molliq.2023.122383.

[45] H. He, Y. Liu, Y. Zhu, T.C. Zhang, S. Yuan, Underoil superhydrophilic CuC_2O_4@Cu-MOFs core-shell nanosheets-coated copper mesh membrane for on-demand emulsion separation and simultaneous removal of soluble dye, Sep. Purif. Technol. 293 (2022) 121089, https://doi.org/10.1016/j.seppur.2022.121089.

[46] D. Tichit, G. Layrac, C. Gérardin, Synthesis of layered double hydroxides through continuous flow processes: a review, Chem. Eng. J. 369 (2019) 302–332, https://doi.org/10.1016/j.cej.2019.03.057.

[47] J.L. Zhuang, D. Ceglarek, S. Pethuraj, A. Terfort, Rapid room-temperature synthesis of metal–organic framework HKUST-1 crystals in bulk and as oriented and patterned thin films, Adv. Funct. Mater. 21 (2011) 1442–1447, https://doi.org/10.1002/adfm.201002529.

[48] N. Al-Janabi, P. Hill, L. Torrente-Murciano, A. Garforth, P. Gorgojo, F. Siperstein, X. Fan, Mapping the Cu-BTC metal–organic framework (HKUST-1) stability envelope in the presence of water vapour for CO_2 adsorption from flue gases, Chem. Eng. J. 281 (2015) 669–677, https://doi.org/10.1016/j.cej.2015.07.020.

[49] M.K. Albolkany, C. Liu, Y. Wang, C.H. Chen, C. Zhu, X. Chen, B. Liu, Molecular surgery at microporous MOF for mesopore generation and renovation, Angew. Chem., Int. Ed. 60 (2021) 14601–14608, https://doi.org/10.1002/anie.202103104.

[50] X. Wang, K. Maeda, A. Thomas, K. Takanabe, G. Xin, J.M. Carlsson, K. Domen, M. Antonietti, A metal-free polymeric photocatalyst for hydrogen production from water under visible light, Nat. Mater. 8 (2009) 76–80, https://doi.org/10.1038/nmat2317.

[51] L. Li, X.L. Liu, M. Gao, W. Hong, G.Z. Liu, L. Fan, B. Hu, Q.H. Xia, L. Liu, G.W. Song, Z.S. Xu, The adsorption on magnetic hybrid Fe_3O_4/HKUST-1/GO of methylene blue from water solution, J. Mater. Chem. A 2 (2014) 1795–1801, https://doi.org/10.1039/c3ta14225f.

[52] Y. Wu, J. Chen, H. Che, X. Gao, Y. Ao, P. Wang, Boosting $2e^-$ oxygen reduction reaction in garland carbon nitride with carbon defects for high-efficient photocatalysis-self-Fenton degradation of 2,4-dichlorophenol, Appl. Catal. B Environ. 307 (2022) 121185, https://doi.org/10.1016/j.apcatb.2022.121185.

[53] G. Majano, O. Martin, M. Hammes, S. Smeets, C. Baerlocher, J. Pérez-Ramírez, Solvent-Mediated reconstruction of the metal–organic framework HKUST-1 ($Cu_3(BTC)_2$), Adv. Funct. Mater. 24 (2014) 3855–3865, https://doi.org/10.1002/adfm.201303678.

[54] L. Sellaoui, F. Edi-Soetaredjo, M. Mohamed, S. Ismadji, B. Ernst, A. Bonilla-Petriciolet, A. Ben Lamine, D. Dell'Angelo, M. Badawi, A novel application of HKUST-1 for textile dyes removal in single and binary solutions: experimental investigation combined with physical modelling, Chem. Eng. J. 480 (2024) 147958, https://doi.org/10.1016/j.cej.2023.147958.

[55] L. Ge, C. Han, Synthesis of MWNTs/g-C_3N_4 composite photocatalysts with efficient visible light photocatalytic hydrogen evolution activity, Appl. Catal. B Environ. 117–118 (2012) 268–274, https://doi.org/10.1016/j.apcatb.2012.01.021.

[56] J. Liu, T. Zhang, Z. Wang, G. Dawson, W. Chen, Simple pyrolysis of urea into graphitic carbon nitride with recyclable adsorption and photocatalytic activity, J. Mater. Chem. 21 (2011) 14398, https://doi.org/10.1039/c1jm12620b.

[57] Y. Wu, X. Li, H. Zhao, F. Yao, J. Cao, Z. Chen, D. Wang, Q. Yang, Core-shell structured Cu_2O@HKUST-1 heterojunction photocatalyst with robust stability for highly efficient tetracycline hydrochloride degradation under visible light, Chem. Eng. J. 426 (2021) 131255, https://doi.org/10.1016/j.cej.2021.131255.

[58] X. Li, B. Kang, F. Dong, Z. Zhang, X. Luo, L. Han, J. Huang, Z. Feng, Z. Chen, J. Xu, B. Peng, Z.L. Wang, Enhanced photocatalytic degradation and H_2/H_2O_2 production performance of S-pCN/$WO_{2.72}$ S-scheme heterojunction with appropriate surface oxygen vacancies, Nano Energy 81 (2021) 105671, https://doi.org/10.1016/j.nanoen.2020.105671.

[59] Y. Zhou, Z. Mao, W. Wang, Z. Yang, X. Liu, In-situ fabrication of graphene oxide hybrid ni-based metal-organic framework (Ni-MOFs@GO) with ultrahigh capacitance as electrochemical pseudocapacitor materials, ACS Appl. Mater. Interfaces 8 (2016) 28904–28916, https://doi.org/10.1021/acsami.6b10640.

[60] X. Song, W. Li, X. Liu, Y. Wu, D. He, Z. Ke, L. Cheng, C. Jiang, G. Wang, X. Xiao, Y. Li, Oxygen vacancies enable the visible light photoactivity of chromium-implanted TiO_2 nanowires, J. Energy Chem. 55 (2021) 154–161, https://doi.org/10.1016/j.jechem.2020.07.013.

[61] G.-Y. Jeong, A.K. Singh, M.-G. Kim, K.-W. Gyak, U. Ryu, K.M. Choi, D.-P. Kim, Metal-organic framework patterns and membranes with heterogeneous pores for flow-assisted switchable separations, Nat. Commun. 9 (2018) 3968, https://doi.org/10.1038/s41467-018-06438-0.

[62] Y. Zeng, N. Guo, H. Li, Q. Wang, X. Xu, Y. Yu, X. Han, H. Yu, Construction of flower-like MoS_2/Ag_2S/Ag Z-scheme photocatalysts with enhanced visible-light photocatalytic activity for water purification, Sci. Total Environ. 659 (2019) 20–32, https://doi.org/10.1016/j.scitotenv.2018.12.333.

[63] Z. Shi, Y. Zhang, G. Duoerkun, W. Cao, T. Liu, L. Zhang, J. Liu, M. Li, Z. Chen, Fabrication of MoS_2/BiOBr heterojunctions on carbon fibers as a weaveable photocatalyst for tetracycline hydrochloride degradation and Cr(VI) reduction under visible light, Environ. Sci.: Nano 7 (2020) 2708–2722, https://doi.org/10.1039/d0en00551g.

[64] D. Jia, Y. Zhang, X. Zhang, P. Feng, L. Yang, R. Ning, H. Pan, Y. Miao, Facile fabrication of Bi nanoparticle-decorated g-C_3N_4 photocatalysts for effective tetracycline hydrochloride degradation: environmental factors, degradation mechanism, pathways and biotoxicity evaluation, Environ. Sci.: Nano 8 (2021) 415–431, https://doi.org/10.1039/d0en01064b.

[65] Y. Xue, Z. Chen, Z. Wu, F. Tian, B. Yu, Hierarchical construction of a new Z-scheme Bi/$BiVO_4$-CdS heterojunction for enhanced visible-light photocatalytic degradation of tetracycline hydrochloride, Sep. Purif. Technol. 275 (2021) 119152, https://doi.org/10.1016/j.seppur.2021.119152.